Nanoscale

MINIREVIEW

View Article Online
View Journal | View Issue

Cite this: *Nanoscale*, 2024, **16**, 12329

Recent advances in synthesis and properties of silver nanoclusters

Xiaolin Liu,†[a,b] Taeyoung Ki,†[a,b] Guocheng Deng,[a,b] Seungwoo Yoo,[a,b] Kangjae Lee,[a,b] Byoung-Hoon Lee,[c] Taeghwan Hyeon *[a,b] and Megalamane S. Bootharaju*[a,b]

Received 25th April 2024,
Accepted 30th May 2024

DOI: 10.1039/d4nr01788a

rsc.li/nanoscale

Achieving atomic precision in nanostructured materials is essential for comprehending formation mechanisms and elucidating structure–property relationships. Within the realm of nanoscience and technology, atomically precise ligand-protected noble metal nanoclusters (NCs) have emerged as a rapidly expanding area of interest. These clusters manifest quantum confinement-induced optoelectronic, photophysical, and chemical properties, along with remarkable catalytic capabilities. Among coinage metals, silver distinguishes itself for the fabrication of stable nanoclusters, primarily due to its cost-effectiveness compared to gold. This minireview provides an overview of recent advancements since 2020 in synthetic methodologies and ligand selections toward attaining NCs boasting a minimum of two free valence electrons. Additionally, it explores strategies for fine-tuning optical properties. The discussion extends to surface reactivity, elucidating how exposure to ligands, heat, and light induces transformations in size and structure. Of paramount significance are the applications of silver NCs in catalytic reactions for energy and chemical conversion, supplemented by in-depth mechanistic insights. Furthermore, the review delineates challenges and outlines future directions in the NC field, with an eye toward the design of new functional materials and prospective applications in diverse technologies, including optoelectronics, energy conversion, and fine chemical synthesis.

1. Introduction

The use of silver traces back to ancient civilizations like Rome and China, valued for its aesthetic allure and believed medicinal properties.[1] Craftsmen combined silver with other metals for decorative brilliance and employed silver vessels to safeguard liquids from contamination. Over the decades, silver has undergone significant advancements, particularly following Faraday's preparation of colloidal gold and its catalytic application by Haruta, which redirected focus towards silver.[2,3] Turkevich's synthesis of analogous silver colloids and Brust's pioneering use of thiolate ligands for surface functionalization and size control of gold nanoparticles further contributed to this evolution.[1] Subsequently, researchers developed synthetic methods for producing atomically monodispersed gold and silver nanoparticles, commonly referred to as atomically precise nanoparticles or nanoclusters (NCs), typically with diameters below 3 nm.[4,5] These NCs, bridging the gap between plasmonic nanoparticles and molecular precursors, offer insights into the evolution of material properties at discrete atom levels.[6–10] Due to quantum confinement effects, NCs exhibit molecule-like optical, photophysical, and chiroptical properties.[11–18] Their high surface-to-volume ratio and defined metal–ligand interface make NCs ideal model catalysts for unravelling molecular-level insights into the origins of catalysis through combined experimental and computational approaches.[19–24]

Among coinage metals, gold has been extensively utilized to investigate the structure–property relationship of gold NCs due to their enhanced stability, facilitating structural characterization *via* single-crystal X-ray crystallography.[1,2] Despite challenges in fabricating stable silver NCs, their lower cost renders them economically competitive, prompting the development of new synthesis strategies.[3] It is noteworthy that silver forms stable Ag(I) clusters with few or no free electrons. Serving as models for metallic nanoparticles, silver NCs with free valence electrons are invaluable for understanding various properties, including identifying the size regime of non-metallic to metallic transitions and emerging plasmonic nanocatalysis.[25–27] Hence, this minireview focuses on the

---

[a] *Center for Nanoparticle Research, Institute for Basic Science (IBS), Seoul 08826, Republic of Korea. E-mail: thyeon@snu.ac.kr, msbootharaju@snu.ac.kr*
[b] *School of Chemical and Biological Engineering, and Institute of Chemical Processes, Seoul National University, Seoul 08826, Republic of Korea*
[c] *KU-KIST Graduate School of Converging Science and Technology, Korea University, Seoul, Republic of Korea*

† These authors contributed equally.

recent advances in ligand-protected Ag NCs possessing free valence electrons since 2020, covering synthetic methodologies, modulation of optical properties, surface reactivity, and promising catalytic applications (Scheme 1). Additionally, we discuss the challenges and future directions in the field of metal NCs.

2. Synthetic strategies

2.1. Ligand-controlled synthesis

The synthesis of ligand-protected metal NCs is typically carried out through the chemical reduction of metal–ligand precursors in appropriate solvents at low or room temperature. Sodium borohydride is commonly employed as a reducing agent.[28–30] Additionally, arylsilane, cyanoborohydride, and borane alkylamine complex are used to control the rate of reduction of metal–ligand complexes and thereby the size and structure of the resultant NCs.[31–35] Understanding the molecular-level mechanism of the formation of NCs is challenging since the reaction solutions involve different phases, disabling the analysis of reaction intermediates through mass spectrometry. Nevertheless, ligands play a critical role in directing the formation of suitable intermediates, which lead to the formation of NCs of a specific size.

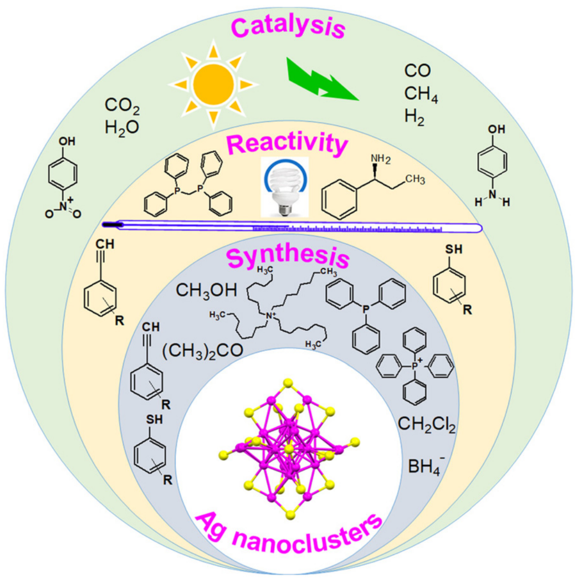

Scheme 1 Schematic illustration of the overall content of the review.

Zhu and co-workers[36] developed a promising synthetic strategy called "dual-level kinetic control", in which the added secondary ligand (phosphine), in addition to the primary thiolate ligand, and the low reaction temperature are found to help achieve first- and second-level kinetic control, respectively. In the absence of a secondary ligand, polydisperse thiolated Ag nanoparticles were obtained. By employing phosphine and diphosphine ligands of different molecular structures, the "dual-level kinetic control" method offers a family of Ag NCs, including $[Ag_{25}(SR)_{18}]^-$, $[Ag_{34}(SR)_{18}(DPPP)_3Cl_4]^{2+}$, $[Ag_{36}(SR)_{26}S_4]^{2+}$, $[Ag_{37}(SR)_{25}Cl_1]^+$, and $[Ag_{52}(SR)_{28}Cl_4]^{2+}$ (Fig. 1) (DPPP: 1,3-bis(diphenylphosphino)propane; SR: 2-adamantanethiolate). In the first-level kinetic control (Fig. 1A), the phosphine ligands retarded the reduction rate, resulting in different Ag NCs correlating with the phosphine ligand type. In the second-level kinetic control (Fig. 1B), lowering the reaction temperature using an ice bath further slowed down the reduction rate, which led to advanced kinetic control and improved synthetic yields of Ag NCs.

By employing various combinations of thiol and diphosphine, a rare collection of super-atomic Ag NCs with sizes Ag_{19}, Ag_{22}, Ag_{26}, and Ag_{30}, possessing 2, 4, 6, and 8 free valence electrons respectively, has been reported.[37]

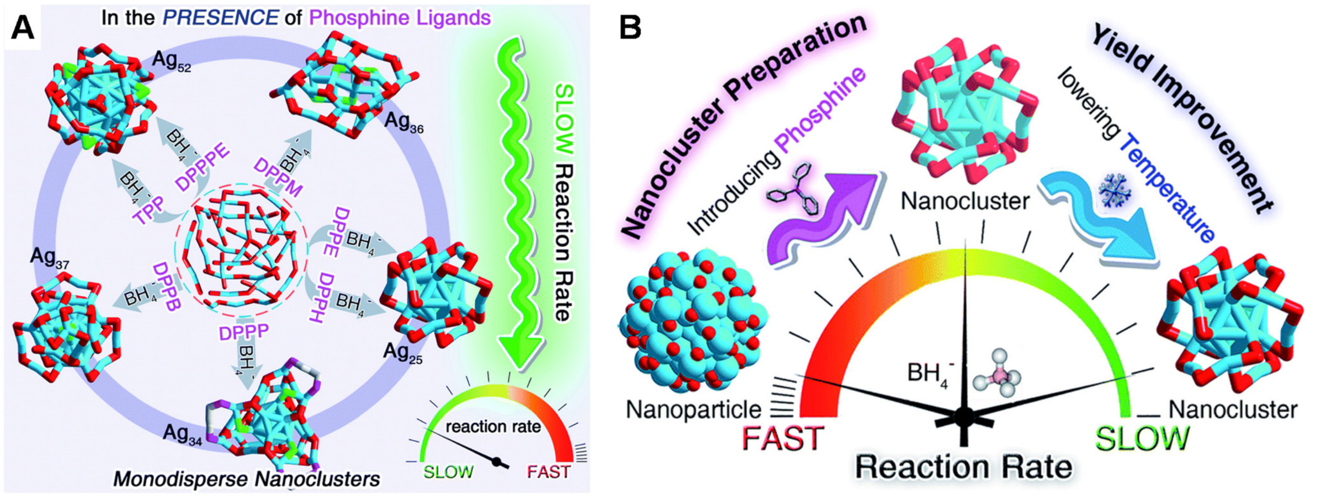

Fig. 1 Schematic illustration of (A) first-level and (B) dual-level kinetic control *via* introducing phosphine ligands and low reaction temperature, leading to synthesis of a series of Ag NCs with improved yields. Reproduced with permission from ref. 36. Copyright (2022).

Interestingly, the cores of these clusters consist of one decahedral Ag_7, perpendicular bidecahedra, three-dimensional pentadecahedra, and hexadecahedra, respectively. The strong structural correlation demonstrates the motif-to-core evolution of the surface Ag (on AgS_2) to construct additional decahedral blocks, offering opportunities to investigate the impact of decahedral evolution patterns on the properties of NCs. In the presence and absence of phosphine ligands, a dithiol is shown to form Ag NCs of different sizes and structures. Specifically, 1,2-benzenedithiolate (1,2-BDT) forms $Ag_{14}(1,2\text{-BDT})_6(PPh_3)_8$ in the presence of PPh_3,[38] while $[Ag_9(1,2\text{-BDT})_6]^{3-}$ forms in the absence of the PPh_3 ligand.[39] The Ag_{14} cluster possesses an inner core of Ag_6 arranged in an octahedral shape, surrounded by an outer cubic shell of Ag_8. Conversely, the Ag atoms of the Ag_9 cluster are arranged in an elongated body-centered cubic format. These examples demonstrate the crucial role of phosphine in the size-selected synthesis of NCs. In contrast, when an isomeric dithiolate, 1,3-benzenedithiolate (1,3-BDT), is used, Ag_{29} NCs are synthesized both in the presence and absence of the PPh_3 ligand.[40] The formation of the Ag_{29} cluster is attributed to its geometrical and electronic stability. However, the presence of PPh_3 facilitates single-crystal growth and increases the yield of Ag_{29} clusters.[40] Notably, the replacement of PPh_3 with diphosphines also yields Ag_{29} clusters.[41]

The Zang group synthesized novel Ag(0)-containing Ag NCs by controlling the molecular structures of auxiliary phosphine ligands while keeping the thiolate ligand unchanged.[42] Specifically, they synthesized $[Ag_{17}(L)_{12}(PPh_3)_6]^{3+}$ (L = quinoline-2-thiol (deprotonated)-4-carboxyl) and $[Ag_{32}(L)_{18}(P(Ph\text{-}pCH_3)_3)_6Cl_2]^{4+}$ (where $P(Ph\text{-}pCH_3)_3$ = tri-*p*-tolylphosphine). The Ag_{17} cluster features an Ag_5 trigonal bipyramid core, while the Ag_{32} cluster has an Ag_{20} inner core formed by the fusion of two Ag_{13} icosahedra. However, both clusters possess surface structures based on $Ag_4L_4P_2$ units and exhibit photoluminescence in the near-infrared region. The rigidity of the surface structure of Ag_{17} results in a higher photoluminescence quantum yield (PLQY: 3.09%) compared to that (less than 0.1%) of Ag_{32}.

2.2. Counterion- and solvent-controlled synthesis

Counterions (cation or anion) are provided to balance the core charge of the NCs, resulting in electrostatic stabilization. Additionally, the bulkiness of the counterion can direct the formation of NCs with specific size and structure. Zang and co-workers[43] observed the unusual cocrystallization of two anionic Ag NCs, $[Ag_{62}(MNT)_{24}(TPP)_6]^{8-}$ and $[Ag_{22}(MNT)_{12}(TPP)_4]^{4-}$ (Fig. 2) (MNT^{2-}: dimercaptomaleonitrile; TPP: triphenylphosphine). The inter- and intra-cluster noncovalent interactions drive the cocrystallization of NCs. Interestingly, when the synthesis is carried out in the presence of positively charged counterions with varied bulkiness, a specific sized NC is obtained. Tetrabutylammonium and tetraphenylphosphonium direct the formation of the truncated-tetrahedral Ag_{22} and the octahedral Ag_{62} NCs, respectively.

The Kang group obtained three medium-sized Ag NCs, namely Ag_{52}, Ag_{54}, and Ag_{58}, co-protected by thiolate, halide, and hydride ligands.[44] The Ag_{52} and Ag_{54} NCs are synthesized in the presence of tetraphenylphosphonium, whereas the Ag_{58} NC is produced in the presence of tetraoctylammonium counterion. The Ag_{52} and Ag_{54} NCs are structurally homologous with respect to the kernel structures and the overall metal-atom configurations, while the Ag_{58} NC has a completely different geometric structure. The formation of different cluster compounds is attributed to the following: (i) the flexibility of the hydrocarbon chain of tetraoctylammonium and the rigidity of the phenyl rings of tetraphenylphosphonium. The different degrees of steric hindrance of the counterions would have resulted in structural rearrangement at distinct levels during the formation of NCs; (ii) different and/or specific interactions among cluster intermediate species and counterions would have remarkably affected the synthesis of NCs of a specific size.

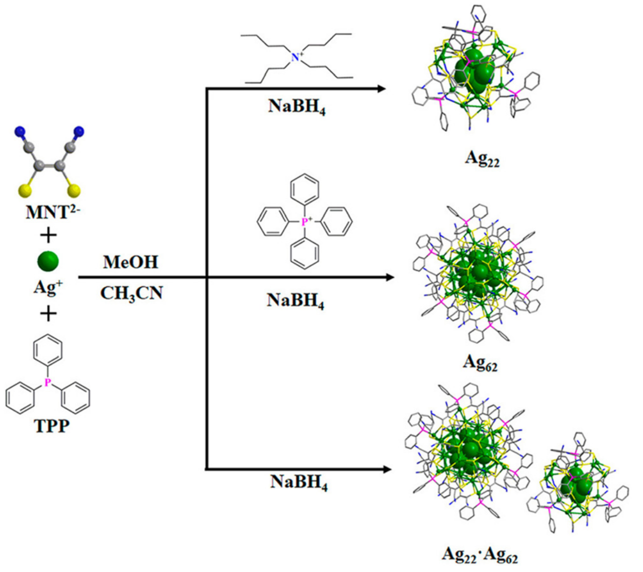

Fig. 2 Synthetic route for counter cation-directed synthesis of $[Ag_{62}(MNT)_{24}(TPP)_6]^{8-}$ and $[Ag_{22}(MNT)_{12}(TPP)_4]^{4-}$ NCs. Color legend: green, Ag; pink, P; yellow, S; blue, N; gray, C. Reproduced with permission from ref. 43. Copyright (2023).

The solvent medium, in which metal–ligand precursors form nuclei and further grow to yield NCs, also plays a crucial role in controlling the size and structure of metal NCs. Organic solvents with varying polarities, such as alcohols (methanol and ethanol), halocarbons (dichloromethane and chloroform), acetonitrile, and dimethylformamide (DMF), are commonly used for the synthesis of Ag NCs since both the precursors and the NC products dissolve well in these solvents. Although the exact reasons for the size selection of NCs are unknown, changing solvents can lead to NCs with distinct structures.

The $[Ag_{30}(TC4A)_4(TBPMT)_8]$ NCs are synthesized in a methanol-chloroform mixture (where $TC4A4^-$ = *p-tert*-butylthiacalix[4]arene; TBPMT = 4-*tert*-butylbenzenemethanethiolate).[45] Interestingly, by replacing methanol in the solvent mixture with acetone, different-sized NCs $[Ag_{34}Na_4Cl_4(TC4A)_4(TBPMT)_{11}(solvents)]^{3+}$ are obtained. The 6-electron-$Ag_{14}{}^{8+}$

kernel of Ag_{30} is formed by the central Ag_6 octahedron sandwiched between two orthogonally oriented Ag_5 trigonal bipyramids through sharing vertices. On the other hand, the 4-electron-$Ag_{10}{}^{6+}$ core of Ag_{34} is formed by two edge-shared octahedrons. These two clusters exhibit distinct optical absorption profiles due to the differences in their geometric and electronic structures. Similarly, *n*-butanol, a rarely used alcohol for the synthesis of NCs, is found to be critical in the synthesis of a large Ag NC $[Ag_{155}(CyS)_{40}(TC4A)_5Cl_2]$ (where CyS = cyclohexanethiolate).[46] The use of other common alcohols is unable to produce this NC. This cluster consists of a metallic core of four concentric shells, $Ag_{13}@Ag_{42}@Ag_{30}@Ag_{70}$. In some instances, special precursors are required to obtain particular clusters. For example, $[Ag(pz)]_n$ (where Hpz = pyrazole) is necessary to obtain the $[Ag_{78}({}^iPrPhS)_{30}(dppm)_{10}Cl_{10}]^{4+}$ cluster.[47] Here, the pz-ligand is not incorporated into the cluster, but its strong coordination effect serves to make $[Ag(pz)]_n$ a controlled-releasing silver ion source. Such ligand-assisted synthesis is applicable to other NCs as well.[48,49] The presence of the halide ligand originates from the *in situ* decomposition of the halocarbon solvent or other sources, a phenomenon also observed in other cluster systems.[35,47,50,51]

2.3. Photochemical and metal-mediated approach

Light serves as a promising energy source for the reduction of noble metal precursors to their metallic state. Inspired by the photochemical synthesis of plasmonic nanoparticles,[52] Zhang and co-workers attempted to synthesize ligand-protected Ag NCs.[53] By irradiating a solution of suitable metal and ligand precursors along with an organic base, they successfully synthesized atomically monodisperse $[Ag_{25}(4\text{-MePhC}{\equiv}C)_{20}(Dpppe)_3]^{3+}$ NCs (as depicted in Fig. 3A) (where Dpppe = 1,5-bis(diphenylphosphino)pentane; 4-MePhC≡CH = 4-methylphenylacetylene). The photochemical formation mechanism of the NCs involves a photoinduced electron-transfer (PET) process. Upon photoexcitation of amines with light wavelength <455 nm, electrons from the amine are transferred to Ag^+ ions, resulting in the oxidation of the amine and the formation of amine N-oxide.

The PET process is supported by experimental and density functional theory results. The absence of light and amine leads to no formation of NCs. A minimum photon energy of 2.7 eV is required to initiate the synthesis of NCs. The structure of Ag_{25} consists of an Ag_{13} core in the form of an anticu-

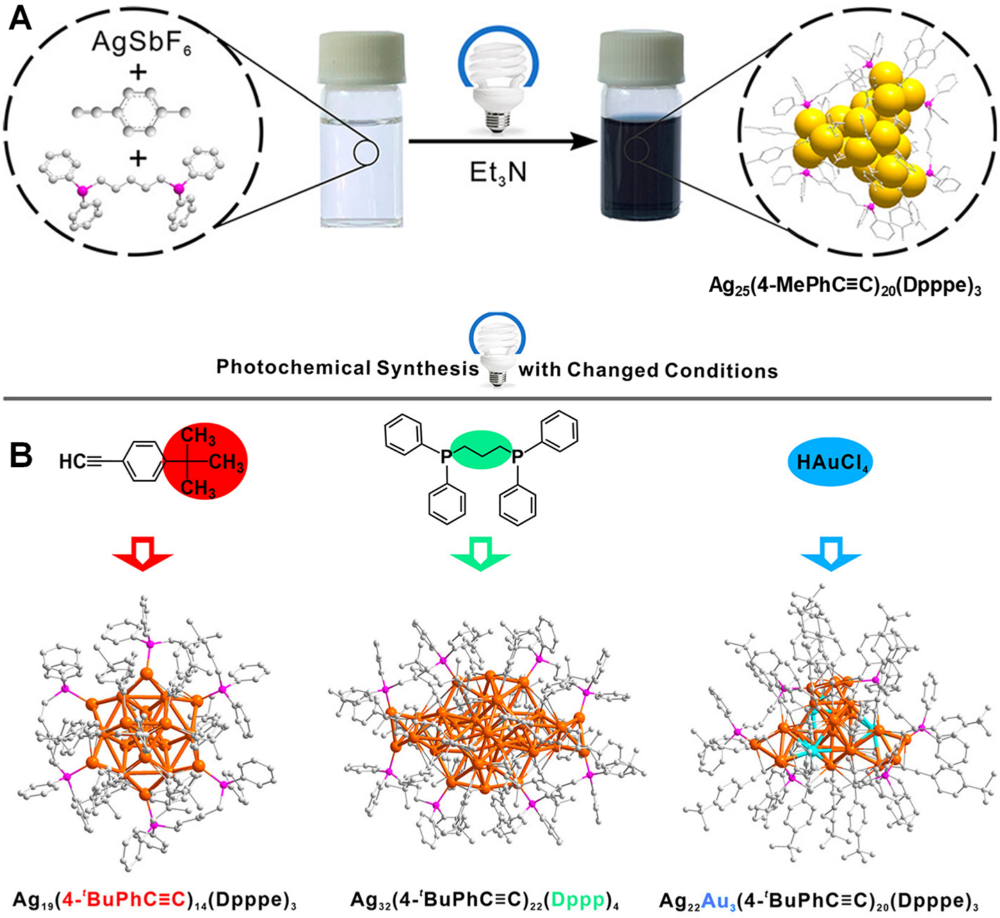

Fig. 3 (A) Schematic illustration of the photochemical synthesis of Ag_{25} NCs by irradiating the precursor solution by <455 nm light for 24 h. (B) Schematic of the photochemical synthesis of Ag NCs of different size, structure and composition. Reproduced with permission from ref. 53. Copyright (2023).

boctahedron, a type of hexagonally close-packed (hcp) lattice. This core differs from the Ag_{13} icosahedral core of thiolated Ag_{25} clusters.[54] This difference likely originates from variations in the coordination modes of thiolate and alkynyl ligands with silver. The remaining 12 Ag atoms form three distorted tetrahedra, which are trigonally distributed around the Ag_{13} core. Subsequently, the metal atoms of the cluster are co-protected by diphosphine and alkynyl ligands. The photochemical method has been found to be applicable to the synthesis of Ag NCs of various sizes and structures by using alkynyl and phosphine ligands with different molecular structures and functionalities (as shown in Fig. 3B). Interestingly, by substituting 4-*tert*-butylphenylacetylene (4-*t*BuPhC≡CH) for 4-MePhC≡CH, $[Ag_{19}(4\text{-}t\text{BuPhC}{\equiv}\text{C})_{14}(\text{Dpppe})_3]^{3+}$ is synthesized with an overall structure similar to that of Ag_{25}. However, the Ag_{19} cluster possesses an Ag_{13} cuboctahedron core unlike the anticuboctahedron Ag_{13} core of the Ag_{25} cluster. Additionally, by introducing 1,3-bis(diphenylphosphino)propane (Dppp), the synthesized product contains $[Ag_{32}(4\text{-}t\text{BuPhC}{\equiv}\text{C})_{22}(\text{Dppp})_4]^{3+}$. The structure of Ag_{32} comprises an Ag_{24} kernel and two distorted Ag_4 tetrahedra. Interestingly, it exhibits electron paramagnetic resonance (EPR) activity due to its 7 free valence electrons. Furthermore, this photochemical route can be used to synthesize alloy NCs, such as $[Ag_{22}Au_3(4\text{-}t\text{BuPhC}{\equiv}\text{C})_{20}(\text{Dpppe})_3]^{3+}$, by introducing corresponding metal precursors.

Attempts to synthesize heteroatom-doped Ag NCs sometimes lead to the formation of undoped Ag NCs, which are only possible in the presence of that particular heterometal atom. For instance, Pd is found to mediate the synthesis of $Ag_{33}(SCH_2CH_2Ph)_{24}(PPh_3)_4$ NC.[55] In its absence or in the presence of Au or Pt, a different sized NC, $Ag_{23}(PPh_3)_8(SC_2H_4Ph)_{18}$, is obtained. Control experiments indicated that $Pd(PPh_3)_4$ is formed first by borohydride reduction, which further catalyzes the reduction of Ag^+ and the growth of the Ag_{33} cluster. Similarly, Cu is found to be essential in synthesizing $Ag_{44}(\text{EBT})_{26}(\text{TPP})_4$ NC (EBT: 2-ethylbenzenethiolate),[56] whose size and core structure are analogous to an all-thiolated $Ag_{44}(SR)_{30}$ cluster. The formation of AgCu alloy NCs is believed to mediate the synthesis of electronically and geometrically stable Ag_{44} clusters. On the other hand, by replacing Cu with Au, AgAu alloy clusters are formed, indicating the unique role of specific metals in the synthesis of certain Ag NCs.

2.4. Other ligands for synthesis of NCs

Coinage metal NCs are typically synthesized using soft-base ligands such as thiolates, phosphines, selenolates, and alkynylides. The use of hard-base ligands with O and N donors is rare because the combination with soft bases is not stable. Recently, the $[Ag_8(\text{pfga})_6]^{6-}$ cluster (pfga: perfluoroglutarate) was synthesized with an unprecedented rhombohedral Ag_8^{6+} core.[57] This two-electron cluster exhibits visible light absorption and emits bright green-yellow light. Following this work, 9-anthracene carboxylate, a bulky monocarboxylate, and different phosphines were used to synthesize two-electron $[Ag_{16}(L)_8(9\text{-AnCO}_2)_{12}]^{2+}$ clusters.[58] Its structure features an $[Ag_8@Ag_8]^{14+}$ core–shell structure, with an $[Ag_8]^{6+}$ superatomic inner core adopting an unprecedented structure showing a distorted hexagonal bipyramidal structure. The outer Ag_8 shell is composed of the unique "$Ag(PR_3)$–AnCOO–$Ag(PR_3)$" staple motifs.

Using N donor ligands, Wang and co-workers synthesized $[Ag_{61}(\text{dpa})_{27}]^{4+}$ (Hdpa = dipyridylamine), the longest silver supercluster based on icosahedral Ag_{13} building blocks with vertex sharing.[59] In this large cluster of clusters, the icosahedron units are bridged by dpa ligands. The quantum size effects contribute significantly to the enhanced metal-related absorptions and the red-shift in the near-infrared region as the length of the cluster increases from 8-electron $[Ag_{21}(\text{dpa})_{12}]^+$ NC to 30-electron $[Ag_{61}(\text{dpa})_{27}]^{4+}$ NC (Fig. 4). Furthermore, electron coupling is developed between constituent Ag_{13} building units. Notably, a disc-like largest structurally characterized Ag cluster of clusters,[31] $[Ag_{93}(PPh_3)_6(C{\equiv}CR)_{50}]^{3+}$ (R = $4\text{-}CH_3OC_6H_4$) is observed for a phosphine and alkynyl combination.

Continuing the use of N donor ligands for Ag NC synthesis, Wang and co-workers[60] designed tetradentate formamidinates and successfully obtained two fcc clusters: $[Ag_{52}(5\text{-F-dpf})_{16}Cl_4]^{2+}$ (5-F-Hdpf = *N*,*N*′-di(5-fluoro-2-pyridinyl)formamidine) and $[Ag_{53}(5\text{-Me-dpf})_{18}]^{5+}$ (5-Me-Hdpf = *N*,*N*′-di(5-methyl-2-pyridinyl)formamidine). All silver atoms are engaged in fcc packing with [111] facets, and no staple motifs are present due to the linear arrangement of the four N donors of the dpf ligands. The Ag_{53} cluster is the largest well-defined [111] facet with 14 fcc Ag atoms. In combination with organic ligands, inorganic ligands such as oxometalates are used to stabilize and tune the cluster size.[61,62] For example, 20-electron Ag NCs such as $Ag_{28}(\text{dppb})_6(MoO_4)_4$, $Ag_{28}(\text{dppb})_6(WO_4)_4$ and $Ag_{32}(\text{dppb})_{12}(MoO_4)_4(NO_3)_4$ (dppb: 1,4-bis(diphenylphosphino)butane) are synthesized through co-protection. Combination of novel multiple ligands can lead to new assembled clusters. For instance, alkynyl, trifluoroacetate, and diphenylphosphinate set forms luminescent one-dimensional high-nuclearity silver polyclusters,[63] such as $[Ag_{16}(C{\equiv}C\textit{t}\text{Bu})_6(\text{tfa})_6(Ph_2PO_2)_4(CH_3OH)]_n$, and $[Ag_{21}(C{\equiv}C\textit{t}\text{Bu})_8(\text{tfa})_6(Ph_2PO_2)_7]_n$.

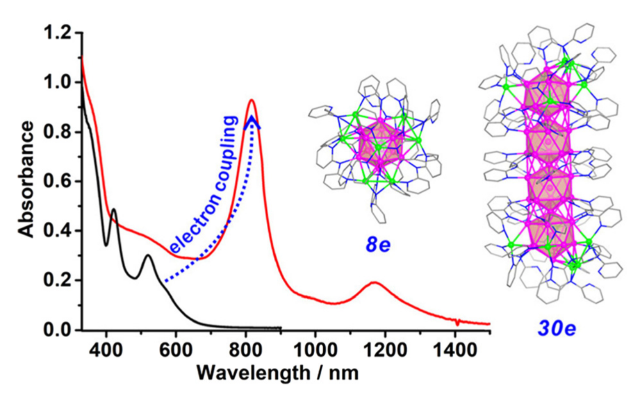

Fig. 4 Optical absorption spectra of $[Ag_{21}(\text{dpa})_{12}]^+$ and $[Ag_{61}(\text{dpa})_{27}]^{4+}$ NCs and corresponding atomic-level structures. Reproduced with permission from ref. 59. Copyright (2021).

2.5. Stability, yield, and functionalization

Metal NCs are typically metastable, which limits their potential applications in optoelectronics and catalysis. For example, the weak Ag–P bonding in the 58-electron $Ag_{64}(P^nBu_3)_{16}Cl_6$ cluster makes the NC unstable.[64] However, the stability of NCs has been significantly improved by employing a combination of ligands. Zhu and co-workers[65] designed a strategy termed "surface environment complication", in which the use of a bidentate PPh_2py ligand with dual (P and N) coordination sites helps stabilize the extremely unstable $Ag_{29}(S\text{-Adm})_{18}(PPh_3)_4$ cluster by forming a new $Ag_{29}(S\text{-Adm})_{15}(NO_3)_3(PPh_2py)_4$ cluster. The Cl intercalation in plasmonic $Ag_{307}Cl_{62}(SPh^tBu)_{110}$ cluster leads to its superstability (stable for a week at 55 °C).[66] Pradeep and co-workers[67] used carboranethiol for the preparation of propeller-shaped $[Ag_{21}(MCT)_{12}(PPh_3)_2]^+$ (MCT: m-carborane-9-thiolate). This cluster is found to be remarkably thermally stable up to 100 °C. The use of macrocyclic ligands in combination with thiolate made the 155-atom Ag NC ultrastable.[46] It exhibits an outstanding photothermal effect. This cluster can attain a temperature of 59.1 °C within 300 s. The heating ability of the cluster remains nearly intact through 6 cycles of heating and cooling processes.

High yields of NCs are crucial for exploring their properties. Since controlling the monodispersity of clusters in large-scale synthesis is challenging, more efforts are indeed required to achieve satisfactory yields. Fast and high-yield (83%) synthesis of $Ag_{44}(SR)_{30}$ clusters is achieved through the development of the CTAB (cetyltrimethylammonium bromide) reverse micelle method.[68] Forming reverse micelles using CTAB to construct a sealed chemical environment is found to be critical in achieving fast and high-yield synthesis. Functionalization of the cluster surface can be useful in improving stability and other properties. Tang and co-workers[69] used a thiophenol ligand with silane substituents, which not only enabled the synthesis of $[Ag_{44}(SPhSi(OEt)_3)_{30}]^{4-}$ clusters but also improved their stability up to 60 °C in air for 13 hours. This silica-coated NCs may be useful in photothermal and photoacoustic imaging applications.

3. Tuning optical properties

The PL of Ag NCs is an attractive characteristic with potential applications in sensing and imaging. It is influenced by several factors, including the metal core, ligand, dopant, solvent, intercluster distance, ion-pairing, and supramolecular interactions, which have been covered in the previous reviews.[70–75] The hydrophilic Ag NCs typically exhibit weak PL due to quenching. To investigate the underlying mechanism of PL quenching in hydrophobic Ag NCs in an aqueous phase, Zhu and colleagues developed a surface functionalization strategy (Fig. 5).[76] Specifically, they synthesized a functionalized $[Ag_{29}(BDTA)_{12}(DPBA)_4]^{3-}$ NC (Ag_{29}-AC; AC denotes all-around-carboxyl functionalization; BDTA: 3,5-dithiolbenzoic acid; DPBA: 4-(diphenylphosphino)benzoic acid) by replacing the unfunctionalized carbon-tail-containing dithiolate and phosphine ligands of $[Ag_{29}(BDT)_{12}(PPh_3)_4]^{3-}$ NC (Ag_{29}-BDT; BDT = 1,3-benzenedithiolate). The water solubility of Ag_{29}-AC, while

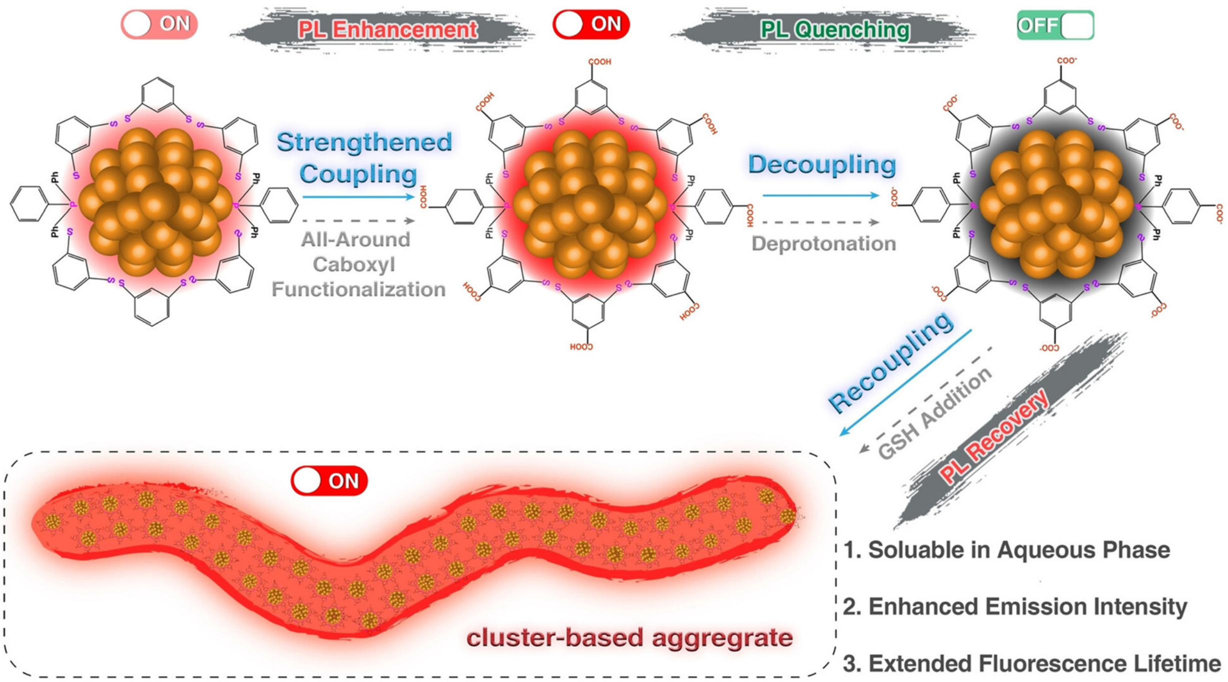

Fig. 5 Schematic of the emission enhancement of the Ag_{29}-AC NC through the strengthened coupling, the emission quenching of Ag_{29}-AC in the aqueous phase caused by molecular decoupling, and the emission recovery of the Ag_{29}-AC NC by its supramolecular recoupling in the presence of reduced glutathione (GSH). Reproduced with permission from ref. 76. Copyright (2024).

retaining its size and structure, allows it to serve as a model NC compound to elucidate the effect of functionalization on PL. The quenching of PL (PLQY: 0.39%; lifetime: 0.21 μs) in Ag_{29}-AC(H_2O) clusters is triggered by phase transfer, leading to molecular decoupling. This increased mobility of Ag_{29}-AC (H_2O) clusters in water weakens the radiative transition. However, the emission recovery of the quenched NCs is achieved (PLQY: 4.7%; lifetime: 2.85 μs) through a supramolecular recoupling route induced by glutathione addition, which promotes the aggregation of NCs. This aggregation restricts intracluster motion and intercluster rotation, thereby strengthening the radiative transition of the clusters.

The selective peripheral modification of $[Ag_{29}(BDT)_{12}(TPP)_4]^{3-}$ NC with Ag(I) complexes, resulting in Ag_{29} + Ag NCs, causes the PL peak to shift from 680 to 770 nm, accompanied by an increase in PLQY from 1.4 to 39%.[77] Despite minor changes in the ground-state geometric and electronic structure, the excited-state properties undergo significant alterations. In addition to the inherent ultrafast intersystem crossing from the S_1 to T_1 state, the Ag_{29} + Ag NC exhibits an additional excited-state relaxation to another triplet state (T'_1) with a time constant of 287 ps. This additional relaxation may be associated with internal motions within the Ag_{29} + Ag NC, such as rearrangement of the ion-pair structure. Such modifications hold promise for applications in photocatalysis.

Ligands and their functional groups modulate the structure and optical absorption features of NCs. The Ag_{14} cluster structure is found to be robust, as it can be formed by a range of thiolate ligands, including monothiol and dithiol.[38] The dithiolated Ag_{14} cluster exhibits unique absorption peaks at 425, 600, and 860 nm, extending into the near-infrared (NIR) region, primarily due to transitions derived from ligands. It also shows dual visible/NIR emission at approximately 680 and 997 nm. Conversely, the monothiolated Ag_{14} cluster has visible absorption peaks at 368 and 530 nm, with yellow PL.[78] Due to the rigidity of the dithiolate, the resulting cluster is thermally robust. Furthermore, the electronic effects of halogen substituents on the thiolate ligand influence the optical and electrochemical bandgap values, governed by intracluster and intercluster π–π interactions.[79] Additionally, the electronegativity of ligand substituents affects ultrafast relaxation dynamics by tuning the electron–phonon interaction.[80] Intracluster interactions among thiolate and diphosphine ligands of Ag_{21} clusters have been shown to enhance the PLQY up to 7%.[81]

In addition to ligands, electron-vibration coupling plays a crucial role in the PL of metal NCs. Weaker and stronger electron-vibration coupling leads to higher and lower NIR PLQY in $Ag_{25}(SR)_{18}$ (3.5%) and $Au_{25}(SR)_{18}$ (1%) clusters, respectively.[82] Doping a single Au atom into Ag_{25} further suppresses the nonradiative decay rate, enhancing PLQY up to 35%.[83] Pradeep and co-workers[84] improved the PL of Ag_{14} NCs co-protected with naphthalenethiol and 1,6-bis(diphenylphosphino)hexane ligands by three-fold through secondary ligand-induced orthogonal self-assembly. The resulting supracolloidal structures, including helical fibers, spheres, and nanosheets, possess restricted intramolecular motion through noncovalent and supramolecular interactions, directly influencing radiative excited-state relaxation. Chiral NCs with light emission exhibit circularly polarized luminescence (CPL). The Zang group synthesized enantiomeric superatomic Ag clusters,[85] $[Ag_{17}(R/S\text{-NYA})_{12}]^{3+}$, stabilized by chiral alkynyl ligands (*R*/*S*-NYA: *N*-((*R*/*S*)-1-(naphthalen-4-yl)ethyl)prop-2-yn-1-amine). They exhibit NIR PLQY of 8% as well as CPL due to the chirality of the excited states.

4. Transformation and surface reactivity

The molecular nature and intermediate stability of NCs render them reactive when subjected to external stimuli such as light, ligands, metal ions, temperature, and others. This reactivity often leads to their conversion into NCs of different sizes, including reduction or growth in size. Thus formed clusters may have novel electronic and geometric structures with exciting optoelectronic and photophysical properties.

4.1. Light-induced transformation

Pradeep and colleagues[86] reported that the $[Ag_{42}(CBDT)_{15}(TPP)_4]^{2-}$ NC undergoes light-activated downsize conversion to form the $Ag_{14}(CBDT)_6(TPP)_6$ cluster (CBDT: *ortho*-carborane-1,2-dithiolate; TPP: triphenylphosphine). Despite the high thermal stability of Ag_{42} cluster up to 200 °C in its solid-state, it undergoes conversion in solution under light irradiation (Fig. 6A). The transformation proceeds through two sets of intermediates (Fig. 6B): (i) $[Ag_{37}(CBDT)_{12}(TPP)_4]^{3-}$ and $[Ag_{35}(CBDT)_8(TPP)_4]^{2-}$ formed after 8 hours, and (ii) $[Ag_{30}(CBDT)_8(TPP)_4]^{2-}$, $[Ag_{26}(CBDT)_{11}(TPP)_4]^{2-}$, and $[Ag_{26}(CBDT)_7(TPP)_7]^{2-}$ formed after 16 hours. After 24 hours, these intermediates transform into the final product, the Ag_{14} cluster. The kernel-centered stable excited states of Ag_{42} are found to be responsible for light-induced cluster conversion. The Ag_{42} cluster emits light at 980 nm with a phosphorescence lifetime of >1.5 μs, whereas Ag_{14} shows red fluorescence emission at 626 nm with a lifetime of 550 ps.

In a recent study, the same group observed a light-activated size-expansion process, wherein the $[Ag_{31}(TRZ)_{10}]^{2-/1-}$ cluster transformed into the $[Ag_{42}(TRZ)_{13}]^{2+}$ cluster (TRZ: 6-(dibutylamino)-1,3,5-triazine-2,4-dithiolate).[87] The size conversion was demonstrated using absorption spectroscopy of NCs with fingerprint absorption features, as well as a clear color change from violet to greenish. The Ag_{31} cluster exhibits photoresponsive behavior, and the resulting intermediate species are covered with solvated electrons, contributing to the expansion of the cluster size. Both the Ag_{31} and Ag_{42} clusters exhibit NIR and red emission, respectively. Notably, the final product Ag_{42} cluster exhibits strikingly short excited-state carrier dynamics compared to the Ag_{31} cluster. In other words, the stable photoexcited-state carriers and unique electronic and geometric structure of the Ag_{31} cluster likely lead to the light-induced size growth of NCs.

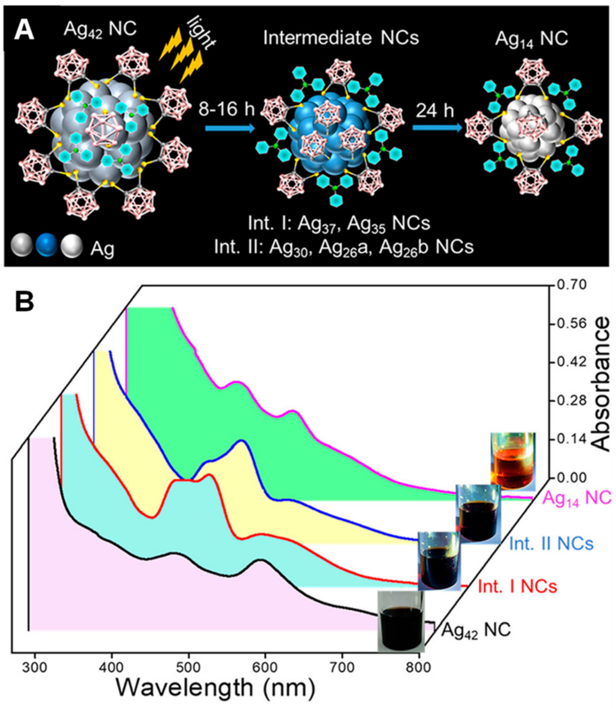

Fig. 6 (A) Schematic of the light-activated conversion of Ag_{42} to Ag_{14} through intermediate clusters. (B) UV–vis absorption spectra of Ag_{42} NC before and after light irradiation along with the mixture of intermediate clusters. Insets: photographs of the color change of cluster solutions during the light-irradiation. Reproduced with permission from ref. 86. Copyright (2021).

4.2. Ligand-exchange-induced transformation

When introduced to a foreign ligand, NCs undergo transformations depending on the inherent electronic effects of the new ligand and the stability of ligand-exchange intermediates. The Zhu group[88] utilized aqueous $Ag_m(SG)_n$ clusters (where SG = L-glutathione) in a biphasic ligand-exchange process with two different thiols (HS^tBu: *tert*-butyl mercaptan; CySH: cyclohexanethiol). This process yielded $Ag_{42}(S^tBu)_{24}$ and $Ag_{61}(SCy)_{40}Cl$. Ag_{42} features a tetrahedral kernel, while Ag_{61} possesses a face-fused bi-tetrahedral Ag_{14} kernel. Interestingly, Ag_{42} can also convert to Ag_{61} through a ligand etching process with excess HSCy. When $Ag_{25}(Capt)_{18}$ NC (Capt: captopril) reacts with 2-isopropylbenzenethiol, the cluster size remains intact,[89] indicating that ligands determine both the cluster size and metal arrangements (*i.e.*, structure). The $[Ag_{18}H_{16}(PPh_3)_{10}]^{2+}$ clusters react with 2-pyrene imine thiol (2-PIT), forming the $[Ag_{35}(2\text{-}PIT)_7(TPP)_7@(H_2O)]^{3+}$ cluster.[90] This cluster emits blue and NIR light under UV excitation due to pyrene-to-metal core charge transfer and charge transfer within the metal core, respectively.

Liu and colleagues[91] observed the formation of a two-electron silver superatom, $Ag_6(S_2P(O^iPr)_2)_4(dppm)_2$, by reacting an eight-electron superatom, $Ag_{20}(S_2P(O^iPr)_2)_{12}$, with a diphosphine (dppm: bis(diphenylphosphino)methane). Here, dppm acts as a chemical scissor, pruning the icosahedron-based Ag_{20} NC to an octahedral Ag_6 NC. The Ag_6 cluster exhibits a bright yellow emission (PLQY: 16.3%) under UV light at room temperature. Sometimes, ligands react with clusters to form even smaller clusters or metal–ligand complex precursors.[92] When $Pt_2Ag_{23}Cl_7(PPh_3)_{10}$ [93] NCs react with a diphosphine ligand dppe (1,2-bis(diphenylphosphino)ethane), a self-assembled $Ag_2Cl_2(dppe)_2$ cluster material is obtained.[94] This material exhibits a high PLQY of ~18% due to metallophilic interactions and crystallization, which restrict intermolecular rotations and minimize nonradiative relaxation paths of the excited-state. Bidentate ligands can assemble the NCs if they have uncoordinated metal sites. The 4,4′-bipyridine (4,4′-bpy) links two two-electron primary building units $Ag_{10}(S_2P(O^iPr)_2)_8$ to make the smallest self-assembled structure of $[Ag_{10}(S_2P(O^iPr)_2)_8]_2(\mu\text{-}4,4'\text{-}bpy)$[95] through N coordination with open Ag site of the cluster. Upon heat treatment, an Ag(I) hydride cluster $Ag_7(H)(S_2P(O^iPr)_2)_6$ undergoes self-redox reaction to produce $Ag_{10}(S_2P(O^iPr)_2)_8$ cluster without addition of any reducing agent.[96] The bicapped trigonal bipyramid metal framework of Ag_7 cluster is well correlated with that of Ag_{10}, suggesting Ag_7 acts as the template in the growth of the cluster.

4.3. Surface reactivity

When a cluster possesses accessible surfaces or labile ligands with bulkiness, it tends to exhibit distinct reactivity, which can be harnessed for specific applications through materials design. For example, the $[Ag_{29}(SSR)_{12}(PPh_3)_4]^{3-}$ cluster is hydrophobic, limiting its utility in applications involving aqueous media. However, the accessible surface and high magnitude of negative electronic charge of this robust cluster enable surface interactions with solvent-conjoined Na^+ cations ($Na_1(NMP)_5$ or $Na_3(DMF)_{12}$) (NMP: *N*-Methyl-2-pyrrolidone).[97] The strong electrostatic attraction between the anionic cluster and these positive ions facilitates the migration of the clusters $[Ag_{29}(SSR)_{12}(PPh_3)_4]^{3-}[Na_1(NMP)_5]_3{}^+$ into the aqueous medium, thus enabling biological applications. Such a micellization strategy has been found to be applicable to most anionic clusters.

Zheng and colleagues[98] synthesized a solvent-coordinated chiral Ag cluster, $[Ag_{14}(SPh(CF_3)_2)_{12}(PPh_3)_4(DMF)_4]$ (Ag_{14}-DMF), in which surface ligands are highly labile. The high surface reactivity of Ag_{14}-DMF allows DMF to dissociate or be exchanged with new ligands. Utilizing the surface reactivity of the cluster, a fully amine-ligated Ag_{14} cluster (where all PPh_3 and DMF are replaced) could be obtained with fine-tuned optical properties by exposing the cluster to excess amine. Interestingly, by introducing chiral amines (*R*-1-PPA: *R*-1-phenylpropylamine and *S*-1-PPA: *S*-1-phenylpropylamine), the racemic Ag_{14}-DMF clusters (Fig. 7A) are converted to homochiral Ag_{14} clusters (Fig. 7B) with a good chiroptical response. By employing bidentate linkers with different chiral configurations,[99] such as (1*R*,2*R*,*N*^{1}*E*,*N*^{2}*E*)-*N*^{1},*N*^{2}-bis(pyridin-3-ylmethylene)cyclohexane-1,2-diamine (LR) and its chiral analog LS, chiral cluster-based metal–organic frameworks are synthesized using Ag_{14}-DMF clusters. These cluster-organic frameworks demonstrate assembly-disassembly process.

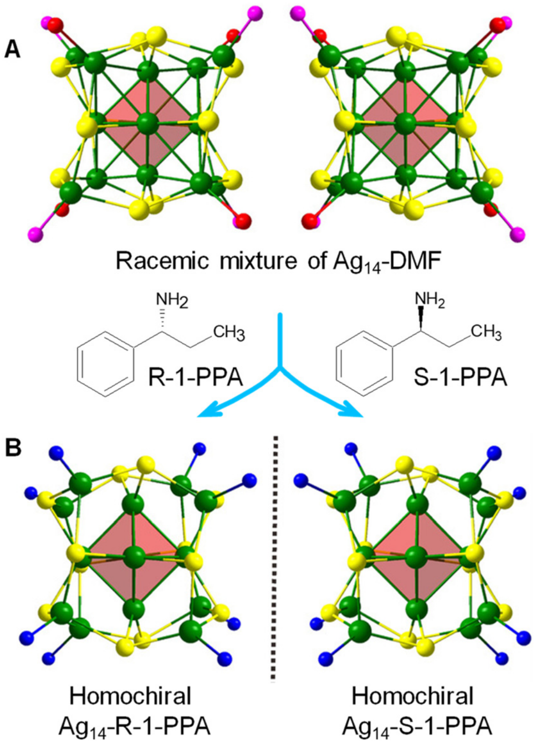

Fig. 7 Core structures of (A) Ag_{14}-DMF enantiomer pair and (B) Ag_{14}-*R*-1-PPA (left) and Ag_{14}-*S*-1-PPA (right). Reproduced with permission from ref. 98. Copyright (2021).

The surface reactivity of NCs with metal ions can also serve as a useful strategy to obtain novel NCs. Zhu and co-workers[100] reported on the role of metal ion quantity in NC transformation. When $[Ag_{25}(2,5\text{-DMBT})_{16}(DPPF)_3]^+$ reacts with less than 0.5 equiv. of Cu^{2+}, size-retained doped clusters $[Ag_{25-x}Cu_x(2,5\text{-DMBT})_{16}(DPPF)_3]^+$ are formed (2,5-DMBT: 2,5-dimethylbenzenethiolate; DPPF: 1,1′-bis(diphenylphosphino)ferrocene). On the other hand, one equiv. of Cu^{2+} results in a structural transformation process, yielding $[Ag_{22-x}Cu_x(2,5\text{-DMBT})_{12}(DPPF)_4Cl_4]^{2+}$ clusters. In the former case, Cu^{2+} acts as a dopant, while in the latter case, it acts as an oxidant. Control experiments demonstrate that Cu^+ forms doped clusters, whereas Cu^{2+} and other common oxidizers produce size-transformed products, indicating the unique role of metal ions in NC reactions.

5. Catalytic applications

Metal NCs with well-defined size, structure, and composition can serve as model nanoparticle analogs to understand the molecular-level mechanisms of catalytic properties. In the following, we will cover various reactions catalyzed by Ag NCs.

5.1. CO_2 conversion

In addressing global energy demands and closing the carbon cycle, CO_2 conversion plays a crucial role. Electrocatalysis holds great potential for converting CO_2 into useful fuels and chemicals using electrical energy produced from renewable sources. Recently, Ag NCs have begun to be utilized for CO_2 reduction. Tang and colleagues[101] synthesized a body-centered cubic (bcc) structured homoleptic $Ag_{15}(C{\equiv}C\text{-}{}^tBu)_{12}{}^+$ cluster and employed it as a catalyst for the electrochemical CO_2 reduction reaction (eCO_2RR). The cluster catalyst exhibits high selectivity for CO, with a highest Faradaic efficiency (FE_{CO}) of 95% at −0.6 V and a maximal turnover frequency of 6.37 s^{-1} at −1.1 V, along with excellent long-term stability. Theoretical calculations indicate that the Ag site created upon stripping a single alkynyl ligand acts as the active site.

In another study, the same group utilized two Ag NCs of identical size, but one was protected by alkynyl ligands and the other was co-protected by thiolate and diphosphine ligands to understand the effect of ligands on eCO_2RR.[102] The clusters are $Ag_{32}L_{24}$ (L = 3,5-bis(trifluoromethylbenzene)acetylide) and $[Ag_{32}(dppe)_5(SR)_{24}]^{2-}$ (SR: trifluoromethylbenzenethiolate). The alkynyl-protected Ag_{32} cluster exhibits a high FE_{CO} of 96.4% at −0.8 V, whereas the thiolated cluster shows an FE_{CO} of only 56.6% at −1.0 V, suggesting the critical role of ligands in eCO_2RR. Theoretical calculations indicate that the energy barrier for the formation of the *COOH intermediate is similar for both clusters. However, the thiolated cluster has the lowest thermodynamic barrier for the formation of H_2 gas (0.05 eV) compared to that (0.51 eV) of the alkynylated cluster, explaining the high CO selectivity in the latter case.

The thiacalix[4]arene-capped 6-electron $[Ag_{30}(TC4A)_4({}^iPrS)_8]$ NC and the chain-like Ag(I) polymer $[H_2Ag_5(TC4A)({}^iPrS)_3]\infty$ are compared with their eCO_2RR performance.[103] The NC exhibits high CO selectivity (93.4% at −0.9 V *versus* RHE) and long-term stability (24 h). Density functional theory (DFT) calculations show that the stabilization of the *COOH intermediate is better on the cluster than on the polymer. Furthermore, the j_{CO} of Ag_{30} is −33.29 mA cm^{-2} at −1.2 V *versus* RHE, which is 2.5 times higher than that of the Ag(I) polymer (−13.2 mA cm^{-2}).

Recently, we have demonstrated that the local hydrophobicity of the surface of NCs influences eCO_2RR by affecting the interfacial water structure.[89] To understand the molecular-level mechanism, two Ag NCs, namely $Ag_{25}(Capt)_{18}$ and $Ag_{25}(IPBT)_{18}$, were synthesized. They exhibit identical metal–ligand arrangements except for the difference in the ligand structure, wherein the carboxyl group of the Capt ligand makes the NC water-soluble, while the isopropyl on the benzene ring of the IPBT ligand makes the NC hydrophobic. Despite loading the NCs on a carbon support, the local hydrophilicity of $Ag_{25}(Capt)_{18}$ is confirmed using contact angle measurements. The eCO_2RR activity of the $Ag_{25}(IPBT)_{18}$ cluster is dramatically enhanced by locally induced hydrophobicity due to bulky alkyl functionality near its surface (Fig. 8A). This enhancement is reflected in the FE_{CO} (90.3%) and higher j_{CO} observed in an H-cell compared to the $Ag_{25}(Capt)_{18}$ cluster with confined hydrophilicity (FE_{CO}: 66.6%) (Fig. 8B). Notably, the hydrophobic Ag_{25} cluster exhibits an impressive j_{CO} as

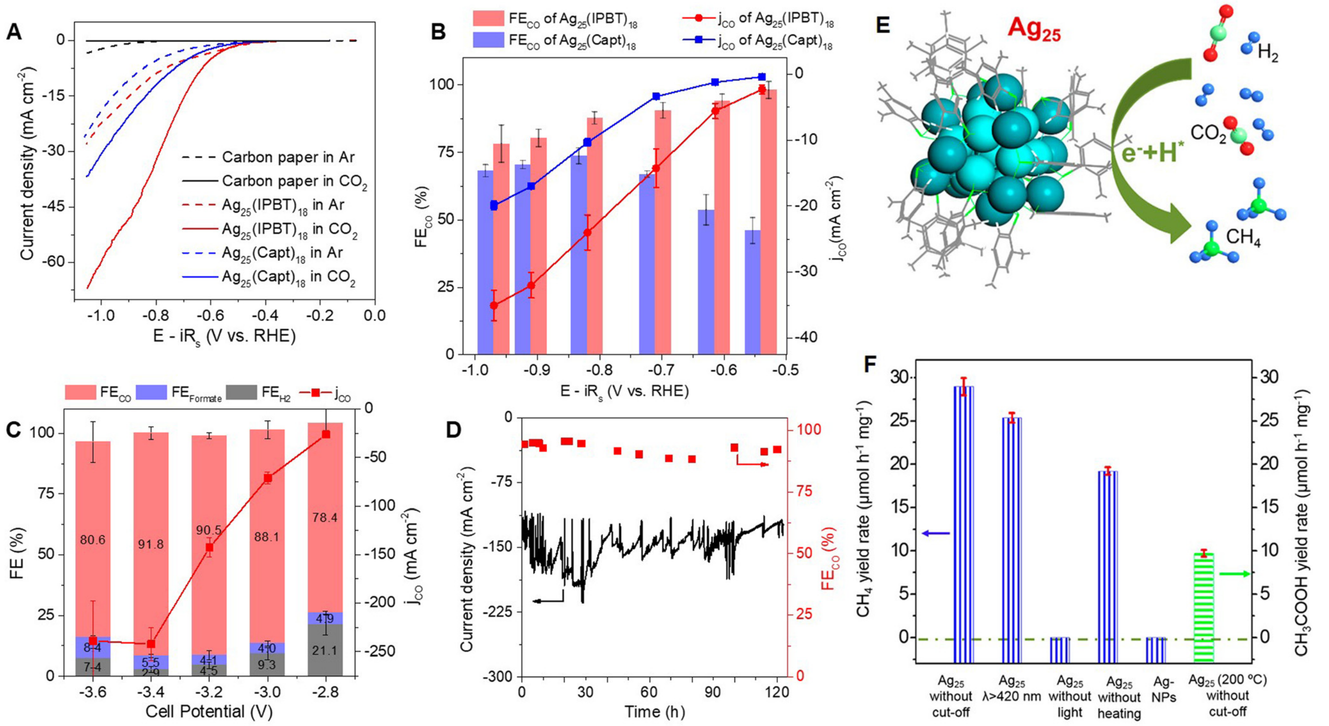

Fig. 8 (A) Polarization curves and (B) FE$_{CO}$ and j_{CO} of Ag$_{25}$(IPBT)$_{18}$ and Ag$_{25}$(Capt)$_{18}$ catalysts in the H-cell. (C) FE$_{CO}$ and j_{CO} of Ag$_{25}$(IPBT)$_{18}$ in the cell potential range from −2.8 to −3.6 V in the MEA cell. (D) Long-term operation of Ag$_{25}$(IPBT)$_{18}$ at −3.2 V cell potential in the MEA cell. Reproduced with permission from ref. 89. Copyright (2024). (E) Structure and photocatalytic CO$_2$ hydrogenation of Ag$_{25}$(DMBT)$_{18}$ cluster. (F) CH$_4$ and CH$_3$COOH yields obtained *via* CO$_2$ hydrogenation over Ag$_{25}$ clusters (CO$_2$: H$_2$ 1 : 3 v/v, 1.5 MPa). Reproduced with permission from ref. 104. Copyright (2021).

high as −240 mA cm^{-2} with FE$_{CO}$ >90% at a cell potential of −3.4 V in a gas-fed membrane electrode assembly device (Fig. 8C). Furthermore, this cluster demonstrates stable eCO$_2$RR activity over a period of 120 hours (Fig. 8D). Operando surface-enhanced infrared absorption spectroscopy and theoretical simulations reveal that the hydrophilic cluster surface accommodates more water molecules due to hydrogen bonding. In contrast, the interfacial water structure on the hydrophobic cluster is similar to bulk water. These differences influence the thermodynamics and kinetics of eCO$_2$RR.

Jin and co-workers[104] utilized the Ag$_{25}$(DMBT)$_{18}$ cluster (DMBT: 2,4-dimethylbenznethiolate) for photocatalytic CO$_2$ hydrogenation (Fig. 8E). The product selectivity is 100% towards CH$_4$ at a relatively mild temperature (100 °C). CO$_2$ adsorption on Ag$_{25}$ is found to be energetically favorable. Operando infrared spectroscopy reveals CO$_2$ methanation proceeds through a –H-assisted multielectron reaction pathway *via* the transformation of formyl and formaldehyde species into surface CH$_x$. CO$_2$ photoreduction is promoted by Ag$_{25}$ clusters, yielding methane at a rate of 28.95 μmol h^{-1} mg^{-1} at 100 °C under Xe lamp illumination without a cutoff filter (Fig. 8F). With a 420 nm cutoff filter, Ag$_{25}$ produces CH$_4$ at a rate of 25.34 μmol h^{-1} mg^{-1}. No activity is observed without light, and heating promotes CO$_2$ photoreduction rate. Interestingly, the selectivity switches from CH$_4$ to acetic acid with a rise in bed temperature. It is suggested that the CO intermediate might bind with Ag–CH$_3$ intermediate at high temperatures (200 °C) to form acetic acid. The Ag NCs stabilized by lacunary polyoxometalates, [Ag$_{24}$(Si$_2$W$_{18}$O$_{66}$)$_3$] and [Ag$_{27}$(Si$_2$W$_{18}$O$_{66}$)$_3$], form HCOOH with 90% selectivity, along with minor products CO and H$_2$.[105] This result indicates that tuning product selectivity may be possible by changing the ligand shell of the NCs.

5.2. Hydrogen evolution

The Pinna group deposited Ag$_{44}$(SR)$_{30}$ NCs onto a wide-bandgap semiconductor TiO$_2$.[106] It produces hydrogen under simulated solar light from water splitting at a rate of 7.4 mmol h^{-1} g$_{catalyst}$$^{-1}$, which is three orders of magnitude higher than under visible light irradiation. The former value is five times higher than that of TiO$_2$ modified with plasmonic Ag nanoparticles, indicating the importance of NCs in photocatalysis. Energy band alignment and transient absorption spectroscopy reveal the formation of a type II heterojunction charge-transfer route under UV-vis irradiation, with the cluster acting as a small bandgap semiconductor. Consequently, clusters function as cocatalysts rather than mere photosensitizers.

Synthesizing core–shell nanomaterials with atomic-level control poses significant challenges despite their potential for enhancing optical and catalytic properties. We reported the synthesis and crystal structure of [Au$_{12}$Ag$_{32}$(SePh)$_{30}$]$^{4-}$, the first instance of selenolated Au–Ag core–shell NCs.[107] These clusters feature a gold icosahedron core encased within a silver dodecahedron, protected by an Ag$_{12}$(SePh)$_{30}$ shell. The presence of the gold core strongly influences the overall electronic structure, leading to synergistic effects that enhance stability and near-infrared-II photoluminescence. Both $Au_{12}Ag_{32}$ and its homometal analog Ag_{44} exhibit strong interactions with oxygen vacancies on TiO_2, facilitating interfacial charge transfer for photocatalysis. Indeed, $Au_{12}Ag_{32}/TiO_2$ demonstrates remarkable solar H_2 production (6810 μmol g^{-1} h^{-1}), surpassing Ag_{44}/TiO_2 and TiO_2 by approximately 6.2 and 37.8 times, respectively (Fig. 9A and B). Furthermore, $Au_{12}Ag_{32}/TiO_2$ exhibits good stability and recyclability with minimal catalytic activity loss (Fig. 9C and D). Experimental and computational findings suggest that $Au_{12}Ag_{32}$ serves as an efficient cocatalyst due to its favorable electronic structure, which aligns well with TiO_2 bands, promoting enhanced separation of photoinduced charge carriers, facilitated by the relatively negatively charged Au_{12} core.

Heteroatom doping may not always have a positive effect on photocatalysis. For instance, when the Ag_{25} cluster is doped with Au and Pd to form isostructural centrally doped $AuAg_{24}$ and $PdAg_{24}$ clusters, respectively, the photocatalytic hydrogen production is lower than that of the parent Ag_{25} cluster.[108] Furthermore, the hydrogen production rate of Ag_{25}/TiO_2 is 10 times higher than that of TiO_2 alone due to the enhanced charge separation at the interface. Measurements using ultraviolet photoelectron spectroscopy and DFT calculations indicate that the lower activities of doped clusters result from an energy mismatch between the levels of doped NCs and TiO_2.

Zhu and co-workers[109] systematically designed an electrocatalytic hydrogen evolution catalyst based on an Ag_{29} cluster by core-alloying with Pt and grafting optimal Mn onto the cluster's surface. In the resulting catalyst, $PtAg_{28}$-BTT-Mn(10), the Mn site exhibits a $\Delta G_H{}^*$ value of 0.18 eV, which is suitable for the hydrogen evolution reaction. This suggests that the Mn sites, rather than the Ag_3 faces of the Ag_{29} cluster, serve as the catalytic sites.

5.3. Nitrate reduction

The Zang group[110] loaded $[Ag_9(mba)_9](NH_4)_9$ NCs onto Ti_3C_2 MXene to form Ag_9/MXene composite catalyst for highly efficient nitrate reduction to ammonia under ambient con-

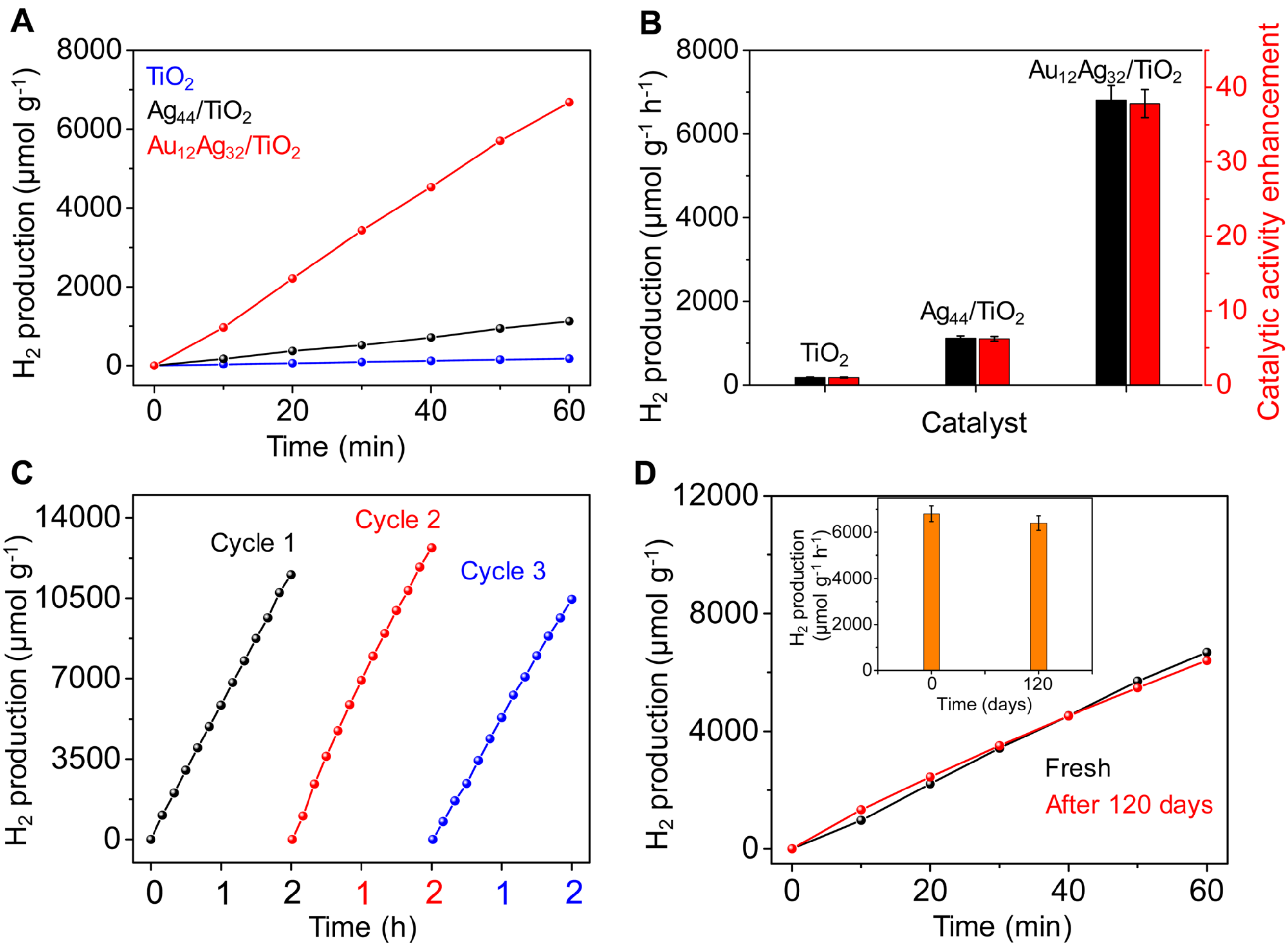

Fig. 9 (A and B) Photocatalytic H_2 production and improvement with Ag_{44}/TiO_2 and $Au_{12}Ag_{32}/TiO_2$ compared to TiO_2. (C) H_2 evolution activity of recycled $Au_{12}Ag_{32}/TiO_2$. (D) H_2 production by fresh and aged $Au_{12}Ag_{32}/TiO_2$. Inset: Bar diagram demonstrating nearly unchanged photocatalytic activity of $Au_{12}Ag_{32}/TiO_2$ clusters after four months of storage. Reproduced with permission from ref. 107. Copyright (2023).

ditions with improved stability in neutral medium. The Ag clusters promote the conversion of nitrate to nitrite. The nitrite-enriched MXene promotes the sustained reaction of nitrite conversion to ammonium ion, establishing a tandem catalytic system. Furthermore, compared to solely Ag_9 NCs, Ag_9/MXene shows enhanced catalytic stability, with no decay in current density after 108 hours of reaction. Tang and colleagues[111] synthesized a homoleptic alkynyl-protected two-electron $[Ag_{30}Pd_4(C_6H_9)_{26}]^{2+}$ cluster and employed it for nitrate to ammonia reduction. The Pd atoms occupy the subcenter of the metal core. This $Ag_{30}Pd_4$ cluster acts as an efficient electrocatalyst for ammonia production with a selectivity of over 90%. *In situ* infrared spectroscopy results show that nitrate to nitrite formation takes place at the silver site, and Pd sites contribute majorly to the nitrite to ammonia conversion. These experimental observations are consistent with DFT calculations, wherein nitrate preferably binds with silver. Upon binding with a water molecule, nitrite is released. This nitrite is then transferred to the vicinally exposed Pd site to complete the reaction. These results demonstrate tandem catalysis of NCs rather than the usually thought synergistic catalysis.

5.4. Other energy related applications

A molecular hybrid of an atomically precise silver NC and polyoxometalates is found to cleave H_2 into protons and electrons, which are stored at the polyoxometalate surface and silver, respectively.[112] The cluster $(Ag_{27})^{17+}$ accommodates electrons by becoming $(Ag_{27})^{13+}$. The polyoxometalate stabilizes the unstable Ag cluster without structural transformation, providing a unique interface for H_2 dissociation and storing protons on its negatively charged basic surface. This example may open new avenues for fuel cell applications. A stable supercapacitor electrode is fabricated using a two-dimensional high-nucleus Ag NC.[113] The high stability of the Ag NC polymer, enabled by its strong coordination with decafluoroazelaic acid (CF2), exhibits a high energy density of 372 F g^{-1} at 4.5 A g^{-1}, along with excellent cycling stability and capacity. This NC demonstrates both high power density and long cycle life, enduring over 6000 cycles with a retention rate of 95%. Additionally, it can tolerate a wide range of scan rates from 5 mV s^{-1} to 1 V s^{-1}, suggesting its potential as a sustainable energy source.

Ag NCs catalyse the hypergolic activity of inert o-carboranealkynyl ligand when they contact with white fuming nitric acid oxidizer.[114] Spontaneous ignition and combustion produce heat, making *o*-carboranealkynyl-protected Ag clusters as potential components of propellant systems. Similarly, Ag cluster-based organic frameworks also exhibit high-performance hypergolic properties.[115] The graphitic carbon nitride (g-C_3N_4)-loaded Ag_{33}(4-MePhC≡C)$_{22}$(Dppp)$_4$ NC serves as excellent photocatalyst for degradation of methyl orange.[116] Compared to pristine g-C_3N_4, the cluster-loaded catalyst shows a 16-fold activity enhancement due to the enhanced separation of photogenerated charge carriers. The co-assembled $[Ag_{29}(BDT)_{12}(TPP)_2]^{3-}$ clusters and $Ru(bpy)_3{}^{2+}$ photosensitizer (*i.e.*, Ag_{29}Ru coassembly) exhibits a greatly enhanced singlet oxygen production capacity under visible light irradiation as compared to pristine Ag_{29} cluster.[117] Narrowing of the HOMO–LUMO gap of the Ag_{29}Ru coassembly is suggested to be the reason for enhancement in singlet oxygen production.

5.5. Organic transformation

The Wang group[118] synthesized two identically sized Ag NCs with different types of ligands, enabling the study of the effect of ligands on the stability and catalytic activity trade-off in the hydrogenation of nitro compounds. The clusters $[Ag_{21}(H_2BTCA)_3(O_2PPh_2)_6]^+$ and $[Ag_{21}(C{\equiv}CC_6H_3\text{-}3,5\text{-}R_2)_6(O_2PPh_2)_{10}]^+$ (Fig. 10A and B, respectively) where H_4BTCA represents *p-tert*-butylthiacalix[4]arene and R represents OMe, possess identical icosahedral kernels. The thiacalix[4]arene-protected Ag_{21} is found to be an 8-electron superatomic cluster, exhibiting robust stability under high temperatures (90 °C) in solution and oxidative conditions (30% H_2O_2). On the other hand, the alkynylated Ag_{21} is a four-electron cluster with an open-shell electronic configuration, demonstrating good ambient stability. However, the alkynylated cluster could catalyse nitrophenol reduction to aminophenol (Fig. 10C) and complete the reaction in 16 minutes (rate constant: 0.228 min^{-1}), while the other cluster could not finish the reaction even after 1.5 hours (rate constant: 0.023 min^{-1}). Notably, the thiacalix[4]arene-protected Ag_{21} shows significantly higher catalytic activity than the catalyst support. These results highlight the importance of the electronic structure of clusters in catalysis, which can be modulated by an appropriate combination of protecting ligands.

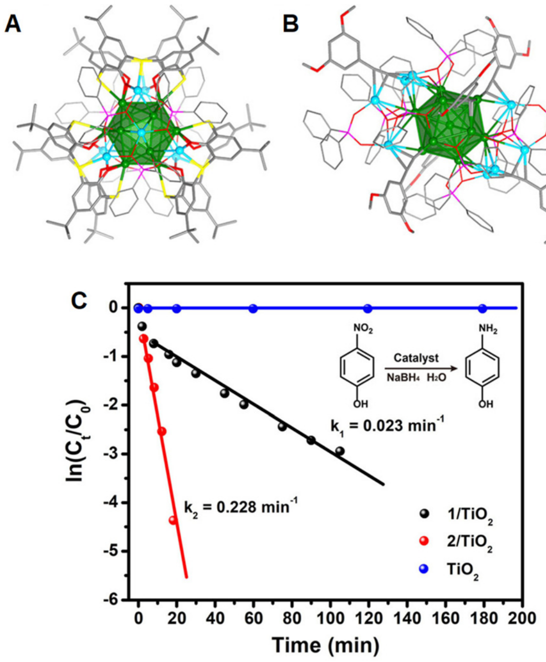

Fig. 10 Molecular structures of (A) thiacalixarene- and (B) alkynyl-protected Ag_{21} NCs. (C) Catalytic activity of Ag_{21}(thiacalixarene)/TiO_2 (1/TiO_2) and Ag_{21}(alkynyl)/TiO_2 (2/TiO_2) and TiO_2 in nitrophenol reduction. Reproduced with permission from ref. 118. Copyright (2022).

The Chen group[119] synthesized three identical $Ag_{33}(SR)_{24}(PPh_3)_4$ NCs with three different thiolate ligands: 2-phenylethanethiol, 4-chlorobenzylmercaptan, and 4-methoxybenzylmercaptan. The benzylthiolated Ag_{33} NCs exhibit superior hydrogenation activity compared to the phenylethanethiolated Ag_{33} cluster. This ligand-dependent catalysis is attributed to the noncovalent (H–π and π–π) interactions of ligands and substrates through phenyl rings, facilitating facile adsorption on the cluster catalyst. Furthermore, the cluster catalysts can be recycled more than five times without significantly losing activity. The surface-exposed Ag_{30} clusters are incorporated into molecular metal oxide cavities,[120] which demonstrate exceptional hydrogenation activities using H_2 gas. The substrate scope is very broad for these cluster catalysts with high yields.

The $Ag_{25}(SR)_{18}$ NCs serve as templates to fabricate AgPd bimetallic nanocatalysts with controlled Pd content and distribution.[121] Initially, the $Ag_{25}(SR)_{18}$ NCs are activated at low temperature, acting as a template for subsequent Pd deposition. By employing low and high amounts of Pd, the location of Pd is manipulated at the subsurface and surface, respectively. The AgPd nanostructure with Pd at the subsurface (12 : 1-Ag : Pd/carbon) exhibits controlled alkyne (2-methyl-3-butyn-2-ol) to alkene (2-methyl-3-buten-2-ol) hydrogenation with 96.6% selectivity. On the other hand, the catalyst with a high Pd content (1 : 6-Ag : Pd/carbon) shows fully hydrogenated products, suggesting the use of Ag NCs in catalyst design. Upon controlled activation of Ag_{25} clusters at 250 °C with an unchanged cluster size,[122] they function as excellent catalysts for styrene oxidation with high selectivity for styrene oxide. However, above this temperature, the clusters sinter to form nanoparticles, and the catalytic performance decreases dramatically with poor styrene oxide selectivity. The Ag_4 NC is synthesized for catalyzing the cyclization of propargylamine with CO_2.[123] The alkyne-captured cluster catalyst intermediate is confirmed by mass spectrometry. This cluster catalyst exhibits a broad substrate scope with high turnover number values and recyclability for several cycles. Furthermore, gram-scale cyclized products could be achieved using the Ag_4 cluster-based catalyst.

6. Summary and perspectives

We have conducted a brief overview of the recent advancements in Ag(0)-containing atomically precise Ag nanoclusters, highlighting the innovative strategies employed in their design and synthesis. By leveraging a rare combination of ligands and meticulously crafting atomic-level structures, researchers have achieved significant progress in enhancing stability, functionalization, and tuning optical and photophysical properties of these nanoclusters. Moreover, the transformative potential of these clusters in catalytic applications, particularly in understanding the role of structures and ligands in catalytic activity and selectivity, has been extensively discussed.

Despite these strides, several challenges remain to be addressed to propel Ag nanocluster research forward. Chief among these is the need to synthesize a greater variety of nanoclusters with consistent size, atomic arrangement, and ligand environment, enabling a comprehensive understanding of their dependency on optical and photophysical characteristics. This necessitates the development of novel synthetic routes (*e.g.*, solid-state[124,125] and biphasic[89] reactions) and the exploration of unconventional precursors, solvents, and reducing agents. Additionally, efforts to upscale synthesis for practical applications must be intensified, requiring advancements in design principles and synthetic chemistry to increase yield and scalability.

The intriguing transformation chemistry of Ag nanoclusters, especially under light-induced conditions, presents an exciting avenue for future exploration. By precisely controlling irradiation parameters and capturing intermediate clusters, researchers can unlock new catalytic possibilities. Furthermore, there is a pressing need to synthesize Ag nanoclusters analogous to existing Au counterparts, such as the elusive $Ag_{38}(SR)_{24}$ analogue, to facilitate comparative studies and expand our understanding of chiroptical and catalytic properties.

While the applications of Ag nanoclusters have been explored to a limited extent, their lower stability compared to gold counterparts presents both challenges and opportunities. The metastability of Ag clusters can be leveraged to create novel catalysts by probing interactions with support materials and elucidating photo-excited-state dynamics. Additionally, the utilization of Ag clusters in CO_2 electrolyzers, owing to their high atom utilization efficiency, holds promise for practical applications. Exploring interactions with other clusters, metal ions, ligands, surfaces, and interfaces will undoubtedly unlock new avenues and possibilities in cluster chemistry. The use of heterometal atoms during the synthesis of silver nanoclusters may lead to either doped silver clusters or novel Ag clusters different from those obtained in the absence of heterometal precursors. Although predicting the choice of heterometal precursors is challenging, considering their ability to form complexes with ligands or transient alloy species may be helpful in assisting the controlled nucleation and growth stages. The heteroatom-doped silver clusters are anticipated to exhibit enhanced catalytic performance and stability due to synergistic and cooperative effects.

In conclusion, the future of cluster chemistry is exceptionally bright, with Ag nanoclusters poised to play a pivotal role in advancing catalysis, energy conversion, and materials science. Continued interdisciplinary efforts and innovative approaches will be essential in harnessing the full potential of these atomically precise nanomaterials.

Conflicts of interest

There are no conflicts to declare.

Acknowledgements

This work was financially supported by the Institute for Basic Science (IBS) with Project Codes IBS-R006-D1 and IBS-R006-Y2.

References

1 I. Chakraborty and T. Pradeep, *Chem. Rev.*, 2017, **117**, 8208–8271.

2 Y. Du, H. Sheng, D. Astruc and M. Zhu, *Chem. Rev.*, 2020, **120**, 526–622.

3 R. Jin, G. Li, S. Sharma, Y. Li and X. Du, *Chem. Rev.*, 2021, **121**, 567–648.

4 M. F. Matus and H. Häkkinen, *Nat. Rev. Mater.*, 2023, **8**, 372–389.

5 Y. Negishi, K. Nobusada and T. Tsukuda, *J. Am. Chem. Soc.*, 2005, **127**, 5261–5270.

6 Z. Wang, M.-D. Li, J.-Y. Shi, H.-F. Su, J.-W. Liu, L. Feng, Z.-Y. Gao, Q.-W. Xue, C.-H. Tung, D. Sun and L.-S. Zheng, *CCS Chem.*, 2022, **4**, 1788–1795.

7 Y.-M. Su, B.-Q. Ji, Z. Wang, S.-S. Zhang, L. Feng, Z.-Y. Gao, Y.-W. Li, C.-H. Tung, D. Sun and L.-S. Zheng, *Sci. China: Chem.*, 2021, **64**, 1482–1486.

8 S.-S. Zhang, R.-C. Liu, X.-C. Zhang, L. Feng, Q.-W. Xue, Z.-Y. Gao, C.-H. Tung and D. Sun, *Sci. China: Chem.*, 2021, **64**, 2118–2124.

9 Z. Wang, Q.-P. Qu, H.-F. Su, P. Huang, R. K. Gupta, Q.-Y. Liu, C.-H. Tung, D. Sun and L.-S. Zheng, *Sci. China: Chem.*, 2020, **63**, 16–20.

10 Z. Wang, H.-F. Su, G.-L. Zhuang, M. Kurmoo, C.-H. Tung, D. Sun and L.-S. Zheng, *CCS Chem.*, 2020, **2**, 663–672.

11 S. Takano and T. Tsukuda, *J. Am. Chem. Soc.*, 2021, **143**, 1683–1698.

12 K. Zheng, X. Yuan and J. Xie, *Chem. Commun.*, 2017, **53**, 9697–9700.

13 H. Lin, X. Song, O. J. H. Chai, Q. Yao, H. Yang and J. Xie, *Adv. Mater.*, 2024, DOI: 10.1002/adma.202401002.

14 X. Liu, J. Chen, J. Yuan, Y. Li, J. Li, S. Zhou, C. Yao, L. Liao, S. Zhuang, Y. Zhao, H. Deng, J. Yang and Z. Wu, *Angew. Chem., Int. Ed.*, 2018, **57**, 11273–11277.

15 N. Xia, J. Yang and Z. Wu, *Nanoscale*, 2015, **7**, 10013–10020.

16 S. Biswas, A. K. Das and S. Mandal, *Acc. Chem. Res.*, 2023, **56**, 1838–1849.

17 G. Deng, K. Lee, H. Deng, M. S. Bootharaju, N. Zheng and T. Hyeon, *J. Phys. Chem. C*, 2022, **126**, 20577–20583.

18 K. Lee, G. Deng, M. S. Bootharaju and T. Hyeon, *Acc. Chem. Res.*, 2023, **56**, 1118–1127.

19 W. Jing, H. Shen, R. Qin, Q. Wu, K. Liu and N. Zheng, *Chem. Rev.*, 2023, **123**, 5948–6002.

20 T. Kawawaki, Y. Kataoka, M. Hirata, Y. Akinaga, R. Takahata, K. Wakamatsu, Y. Fujiki, M. Kataoka, S. Kikkawa, A. S. Alotabi, S. Hossain, D. J. Osborn, T. Teranishi, G. G. Andersson, G. F. Metha, S. Yamazoe and Y. Negishi, *Angew. Chem., Int. Ed.*, 2021, **60**, 21340–21350.

21 T. Kawawaki, T. Okada, D. Hirayama and Y. Negishi, *Green Chem.*, 2024, **26**, 122–163.

22 A. K. Das, S. Biswas, A. Pal, S. S. Manna, A. Sardar, P. K. Mondal, B. Sahoo, B. Pathak and S. Mandal, *Nanoscale*, 2024, **16**, 3583–3590.

23 Y. Yun, H. Sheng, K. Bao, L. Xu, Y. Zhang, D. Astruc and M. Zhu, *J. Am. Chem. Soc.*, 2020, **142**, 4126–4130.

24 S. Wang, S. Jin, S. Yang, S. Chen, Y. Song, J. Zhang and M. Zhu, *Sci. Adv.*, 2015, **1**, e1500441.

25 A. Desireddy, B. E. Conn, J. Guo, B. Yoon, R. N. Barnett, B. M. Monahan, K. Kirschbaum, W. P. Griffith, R. L. Whetten, U. Landman and T. P. Bigioni, *Nature*, 2013, **501**, 399–402.

26 H. Yang, Y. Wang, H. Huang, L. Gell, L. Lehtovaara, S. Malola, H. Häkkinen and N. Zheng, *Nat. Commun.*, 2013, **4**, 2422.

27 H. Chang, M. S. Bootharaju, S. Lee, J. H. Kim, B. H. Kim and T. Hyeon, *Bull. Korean Chem. Soc.*, 2021, **42**, 1386–1399.

28 X.-H. Ma, Y. Si, L.-L. Luo, Z.-Y. Wang, S.-Q. Zang and T. C. W. Mak, *ACS Nano*, 2022, **16**, 5507–5514.

29 X. Ma, Y. Bai, Y. Song, Q. Li, Y. Lv, H. Zhang, H. Yu and M. Zhu, *Angew. Chem., Int. Ed.*, 2020, **59**, 17234–17238.

30 G. Deng, T. Ki, S. Yoo, X. Liu, K. Lee, M. S. Bootharaju and T. Hyeon, *Nanoscale*, 2024, DOI: 10.1039/D4NR01471E.

31 F. Hu, R.-L. He, Z.-J. Guan, C.-Y. Liu and Q.-M. Wang, *Angew. Chem., Int. Ed.*, 2023, **62**, e202304134.

32 G. Deng, H. Yun, M. S. Bootharaju, F. Sun, K. Lee, X. Liu, S. Yoo, Q. Tang, Y. J. Hwang and T. Hyeon, *J. Am. Chem. Soc.*, 2023, **145**, 27407–27414.

33 G. Deng, J. Kim, M. S. Bootharaju, F. Sun, K. Lee, Q. Tang, Y. J. Hwang and T. Hyeon, *J. Am. Chem. Soc.*, 2023, **145**, 3401–3407.

34 G. Deng, T. Ki, X. Liu, Y. Chen, K. Lee, S. Yoo, Q. Tang, M. S. Bootharaju and T. Hyeon, *Chem. Commun.*, 2024, **60**, 1289–1292.

35 F. Hu, J.-J. Li, Z.-J. Guan, S.-F. Yuan and Q.-M. Wang, *Angew. Chem., Int. Ed.*, 2020, **59**, 5312–5315.

36 X. Wei, C. Xu, H. Li, X. Kang and M. Zhu, *Chem. Sci.*, 2022, **13**, 5531–5538.

37 X. Ma, S. He, Q. Li, Q. Li, J. Chai, W. Ma, G. Li, H. Yu and M. Zhu, *Inorg. Chem.*, 2023, **62**, 15680–15687.

38 M. Bodiuzzaman, E. Khatun, K. S. Sugi, G. Paramasivam, W. A. Dar, S. Antharjanam and T. Pradeep, *J. Phys. Chem. C*, 2020, **124**, 23426–23432.

39 B. J. Alamer, M. S. Bootharaju, S. M. Kozlov, Z. Cao, A. Shkurenko, S. Nematulloev, P. Maity, O. F. Mohammed, M. Eddaoudi, L. Cavallo, J.-M. Basset and O. M. Bakr, *Inorg. Chem.*, 2021, **60**, 4306–4312.

40 L. G. AbdulHalim, M. S. Bootharaju, Q. Tang, S. Del Gobbo, R. G. AbdulHalim, M. Eddaoudi, D.-e. Jiang and O. M. Bakr, *J. Am. Chem. Soc.*, 2015, **137**, 11970–11975.

41 E. Khatun, A. Ghosh, P. Chakraborty, P. Singh, M. Bodiuzzaman, P. Ganesan, G. Nataranjan, J. Ghosh, S. K. Pal and T. Pradeep, *Nanoscale*, 2018, **10**, 20033–20042.

42 Q.-Q. Ma, X.-J. Zhai, J.-H. Huang, Y. Si, X.-Y. Dong, S.-Q. Zang and T. C. W. Mak, *Nanoscale*, 2024, **16**, 9361–9366.

43 Y. Li, X.-M. Luo, P. Luo, Q.-X. Zang, Z.-Y. Wang and S.-Q. Zang, *ACS Nano*, 2023, **17**, 5834–5841.

44 H. Li, X. Wei, X. Kang and M. Zhu, *Nanoscale*, 2024, **16**, 1254–1259.

45 Z. Wang, H. Zhao, Y.-Z. Li, C. Zhang, R. K. Gupta, C.-H. Tung and D. Sun, *Nano Lett.*, 2024, **24**, 458–465.

46 Z. Wang, F. Alkan, C. M. Aikens, M. Kurmoo, Z.-Y. Zhang, K.-P. Song, C.-H. Tung and D. Sun, *Angew. Chem., Int. Ed.*, 2022, **61**, e202206742.

47 W.-J. Zhang, Z. Liu, K.-P. Song, C. M. Aikens, S.-S. Zhang, Z. Wang, C.-H. Tung and D. Sun, *Angew. Chem., Int. Ed.*, 2021, **60**, 4231–4237.

48 M. S. Bootharaju, H. Chang, G. Deng, S. Malola, W. Baek, H. Häkkinen, N. Zheng and T. Hyeon, *J. Am. Chem. Soc.*, 2019, **141**, 8422–8425.

49 M. Qu, H. Li, L.-H. Xie, S.-T. Yan, J.-R. Li, J.-H. Wang, C.-Y. Wei, Y.-W. Wu and X.-M. Zhang, *J. Am. Chem. Soc.*, 2017, **139**, 12346–12349.

50 M. S. Bootharaju, W. Baek, G. Deng, K. Singh, O. Voznyy, N. Zheng and T. Hyeon, *Chem*, 2022, **8**, 2978–2989.

51 A. Gonzàlez-Rosell, S. Malola, R. Guha, N. R. Arevalos, M. F. Matus, M. E. Goulet, E. Haapaniemi, B. B. Katz, T. Vosch, J. Kondo, H. Häkkinen and S. M. Copp, *J. Am. Chem. Soc.*, 2023, **145**, 10721–10729.

52 L. Maretti, P. S. Billone, Y. Liu and J. C. Scaiano, *J. Am. Chem. Soc.*, 2009, **131**, 13972–13980.

53 Y.-X. Wang, J. Zhang, H.-F. Su, X. Cui, C.-Y. Wei, H. Li and X.-M. Zhang, *ACS Nano*, 2023, **17**, 11607–11615.

54 C. P. Joshi, M. S. Bootharaju, M. J. Alhilaly and O. M. Bakr, *J. Am. Chem. Soc.*, 2015, **137**, 11578–11581.

55 F. Tian and R. Chen, *J. Am. Chem. Soc.*, 2019, **141**, 7107–7114.

56 M. S. Bootharaju, S. Lee, G. Deng, S. Malola, W. Baek, H. Häkkinen, N. Zheng and T. Hyeon, *Angew. Chem., Int. Ed.*, 2021, **60**, 9038–9044.

57 K.-G. Liu, X.-M. Gao, T. Liu, M.-L. Hu and D.-e. Jiang, *J. Am. Chem. Soc.*, 2020, **142**, 16905–16909.

58 H.-H. Wang, J. Wei, F. Bigdeli, F. Rouhani, H.-F. Su, L.-X. Wang, S. Kahlal, J.-F. Halet, J.-Y. Saillard, A. Morsali and K.-G. Liu, *Nanoscale*, 2023, **15**, 8245–8254.

59 S.-F. Yuan, C.-Q. Xu, W.-D. Liu, J.-X. Zhang, J. Li and Q.-M. Wang, *J. Am. Chem. Soc.*, 2021, **143**, 12261–12267.

60 F. Hu, H.-W. Luyang, R.-L. He, Z.-J. Guan, S.-F. Yuan and Q.-M. Wang, *J. Am. Chem. Soc.*, 2022, **144**, 19365–19371.

61 G.-X. Duan, J. Han, B.-Z. Yang, Y.-P. Xie and X. Lu, *Nanoscale*, 2020, **12**, 1617–1622.

62 S.-S. Zhang, F. Alkan, H.-F. Su, C. M. Aikens, C.-H. Tung and D. Sun, *J. Am. Chem. Soc.*, 2019, **141**, 4460–4467.

63 J. Wei, F. Bigdeli, L.-X. Wang, L.-L. Hou, A. Panjehpour, Y. Ma, K.-Z. Wang, A. Morsali and K.-G. Liu, *Inorg. Chem.*, 2023, **62**, 10185–10192.

64 M. Diecke, C. Schrenk and A. Schnepf, *Angew. Chem., Int. Ed.*, 2020, **59**, 14418–14422.

65 C. Xu, Q. Yuan, X. Wei, H. Li, H. Shen, X. Kang and M. Zhu, *Chem. Sci.*, 2022, **13**, 1382–1389.

66 M.-X. Ma, X.-L. Ma, G.-M. Liang, X.-T. Shen, Q.-L. Ni, L.-C. Gui, X.-J. Wang, S.-Y. Huang and S.-M. Li, *J. Am. Chem. Soc.*, 2021, **143**, 13731–13737.

67 A. Jana, P. M. Unnikrishnan, A. K. Poonia, J. Roy, M. Jash, G. Paramasivam, J. Machacek, K. N. V. D. Adarsh, T. Base and T. Pradeep, *Inorg. Chem.*, 2022, **61**, 8593–8603.

68 L. Qin, F. Zhang, X. Ma, Y. Tang, G. Ma and Z. Tang, *Dalton Trans.*, 2021, **50**, 562–567.

69 J. Yang, S. Xie, H. Zhang, W. Xu, A. Dong and Y. Tang, *Chem. Commun.*, 2022, **58**, 6849–6852.

70 J. Yang and R. Jin, *J. Phys. Chem. C*, 2021, **125**, 2619–2625.

71 X. Kang and M. Zhu, *Chem. Soc. Rev.*, 2019, **48**, 2422–2457.

72 S. Wang, X. Meng, A. Das, T. Li, Y. Song, T. Cao, X. Zhu, M. Zhu and R. Jin, *Angew. Chem., Int. Ed.*, 2014, **53**, 2376–2380.

73 X. Wang, B. Yin, L. Jiang, C. Yang, Y. Liu, G. Zou, S. Chen and M. Zhu, *Science*, 2023, **381**, 784–790.

74 S. Chen, W. Du, C. Qin, D. Liu, L. Tang, Y. Liu, S. Wang and M. Zhu, *Angew. Chem., Int. Ed.*, 2020, **59**, 7542–7547.

75 M. S. Bootharaju, S. M. Kozlov, Z. Cao, A. Shkurenko, A. M. El-Zohry, O. F. Mohammed, M. Eddaoudi, O. M. Bakr, L. Cavallo and J.-M. Basset, *Chem. Mater.*, 2018, **30**, 2719–2725.

76 H. Shen, J. Xu, Z. Fu, X. Wei, X. Kang, W. Shi and M. Zhu, *Angew. Chem., Int. Ed.*, 2024, **63**, e202317995.

77 W. Ishii, Y. Okayasu, Y. Kobayashi, R. Tanaka, S. Katao, Y. Nishikawa, T. Kawai and T. Nakashima, *J. Am. Chem. Soc.*, 2023, **145**, 11236–11244.

78 H. Yang, J. Lei, B. Wu, Y. Wang, M. Zhou, A. Xia, L. Zheng and N. Zheng, *Chem. Commun.*, 2013, **49**, 300–302.

79 A. K. Das, R. Mekkat, S. Maity, A. S. Nair, S. Bhandary, R. Bhowal, A. Patra, B. Pathak, D. Chopra and S. Mandal, *Inorg. Chem.*, 2021, **60**, 19270–19277.

80 S. Kolay, S. Maity, S. Chakraborty, S. Ghosh and A. Patra, *J. Phys. Chem. C*, 2023, **127**, 3769–3777.

81 S. Kolay, S. Chakraborty, S. Pramanik and A. Patra, *J. Phys. Chem. C*, 2024, **128**, 7643–7651.

82 Z. Liu, M. Zhou, L. Luo, Y. Wang, E. Kahng and R. Jin, *J. Am. Chem. Soc.*, 2023, **145**, 19969–19981.

83 M. S. Bootharaju, C. P. Joshi, M. R. Parida, O. F. Mohammed and O. M. Bakr, *Angew. Chem., Int. Ed.*, 2016, **55**, 922–926.

84 K. S. Sugi, A. P. Sandra, Nonappa, D. Ghosh, J. S. Mohanty, M. Paulthangam Kannan, B. S. Sooraj, P. Srikrishnarka, J. Roy, W. A. Dar and T. Pradeep, *Nanoscale*, 2023, **15**, 11927–11934.

85 M.-M. Zhang, X.-Y. Dong, Z.-Y. Wang, X.-M. Luo, J.-H. Huang, S.-Q. Zang and T. C. W. Mak, *J. Am. Chem. Soc.*, 2021, **143**, 6048–6053.

86 A. Jana, M. Jash, A. K. Poonia, G. Paramasivam, M. R. Islam, P. Chakraborty, S. Antharjanam, J. Machacek, S. Ghosh, K. N. V. D. Adarsh, T. Base and T. Pradeep, *ACS Nano*, 2021, **15**, 15781–15793.

87 A. Jana, W. A. Dar, S. K. Jana, A. K. Poonia, V. Yadav, J. Roy, S. Chandra, K. N. V. D. Adarsh, R. H. A. Ras and T. Pradeep, *Chem. Mater.*, 2023, **35**, 7020–7031.

88 T. Chen, S. Yang, Y. Song, J. Chai, Q. Li, X. Ma, G. Li, H. Yu and M. Zhu, *Chem. Commun.*, 2020, **56**, 7605–7608.

89 S. Yoo, S. Yoo, G. Deng, F. Sun, K. Lee, H. Jang, C. W. Lee, X. Liu, J. Jang, Q. Tang, Y. J. Hwang, T. Hyeon and M. S. Bootharaju, *Adv. Mater.*, 2024, **36**, 2313032.
90 A. Jana, P. Chakraborty, W. A. Dar, S. Chandra, E. Khatun, M. P. Kannan, R. H. A. Ras and T. Pradeep, *Chem. Commun.*, 2020, **56**, 12550–12553.
91 Y.-M. Tseng, J.-H. Liao, T.-H. Chiu, H. Liang, S. Kahlal, J.-Y. Saillard and C. W. Liu, *Inorg. Chem.*, 2023, **62**, 3866–3874.
92 A. Baksi, M. S. Bootharaju, P. K. Chhotaray, P. Chakraborty, B. Mondal, S. Bhat, R. Gardas and T. Pradeep, *J. Phys. Chem. C*, 2017, **121**, 26483–26492.
93 M. S. Bootharaju, S. M. Kozlov, Z. Cao, M. Harb, N. Maity, A. Shkurenko, M. R. Parida, M. N. Hedhili, M. Eddaoudi, O. F. Mohammed, O. M. Bakr, L. Cavallo and J.-M. Basset, *J. Am. Chem. Soc.*, 2017, **139**, 1053–1056.
94 M. S. Bootharaju, S. Lee, G. Deng, H. Chang, W. Baek and T. Hyeon, *J. Chem. Phys.*, 2021, **155**, 014307.
95 W.-J. Yen, J.-H. Liao, T.-H. Chiu, Y.-S. Wen and C. W. Liu, *Inorg. Chem.*, 2024, **63**, 5320–5324.
96 Y.-J. Zhong, J.-H. Liao, T.-H. Chiu, S. Kahlal, C.-J. Lin, J.-Y. Saillard and C. W. Liu, *Angew. Chem., Int. Ed.*, 2021, **60**, 12712–12716.
97 X. Kang, X. Wei, P. Xiang, X. Tian, Z. Zuo, F. Song, S. Wang and M. Zhu, *Chem. Sci.*, 2020, **11**, 4808–4816.
98 G. Deng, S. Malola, P. Yuan, X. Liu, B. K. Teo, H. Häkkinen and N. Zheng, *Angew. Chem., Int. Ed.*, 2021, **60**, 12897–12903.
99 G. Deng, B. K. Teo and N. Zheng, *J. Am. Chem. Soc.*, 2021, **143**, 10214–10220.
100 S. Wang, Y. Tan, T. Li, Q. Zhou, P. Li, S. Yang, H. Yu and M. Zhu, *Inorg. Chem.*, 2022, **61**, 18450–18457.
101 L. Qin, F. Sun, X. Ma, G. Ma, Y. Tang, L. Wang, Q. Tang, R. Jin and Z. Tang, *Angew. Chem., Int. Ed.*, 2021, **60**, 26136–26141.
102 L. Chen, F. Sun, Q. Shen, L. Qin, Y. Liu, L. Qiao, Q. Tang, L. Wang and Z. Tang, *Nano Res.*, 2022, **15**, 8908–8913.
103 L.-J. Li, Y.-T. Luo, Y.-Q. Tian, P. Wang, X.-Y. Yi, J. Yan, Y. Pei and C. Liu, *Inorg. Chem.*, 2023, **62**, 14377–14384.
104 Y. Xiong, H. Chen, Y. Hu, S. Yang, X. Xue, L. He, X. Liu, J. Ma and Z. Jin, *Nano Lett.*, 2021, **21**, 8693–8700.
105 Y. Feng, F. Fu, L. Zeng, M. Zhao, X. Xin, J. Liang, M. Zhou, X. Fang, H. Lv and G.-Y. Yang, *Angew. Chem., Int. Ed.*, 2024, **63**, e202317341.
106 Y. Wang, X.-H. Liu, Q. Wang, M. Quick, S. A. Kovalenko, Q.-Y. Chen, N. Koch and N. Pinna, *Angew. Chem., Int. Ed.*, 2020, **59**, 7748–7754.
107 M. S. Bootharaju, C. W. Lee, G. Deng, H. Kim, K. Lee, S. Lee, H. Chang, S. Lee, Y.-E. Sung, J. S. Yoo, N. Zheng and T. Hyeon, *Adv. Mater.*, 2023, **35**, 2207765.
108 Y. Liu, D. Long, A. Springer, R. Wang, N. Koch, M. Schwalbe, N. Pinna and Y. Wang, *Sol. RRL*, 2023, **7**, 2201057.
109 H. Shen, Q. Zhu, J. Xu, K. Ni, X. Wei, Y. Du, S. Gao, X. Kang and M. Zhu, *Nanoscale*, 2023, **15**, 14941–14948.
110 L. Liu, S.-J. Zheng, H. Chen, J. Cai and S.-Q. Zang, *Angew. Chem., Int. Ed.*, 2024, **63**, e202316910.
111 L. Qin, F. Sun, Z. Gong, G. Ma, Y. Chen, Q. Tang, L. Qiao, R. Wang, Z.-Q. Liu and Z. Tang, *ACS Nano*, 2023, **17**, 12747–12758.
112 K. Yonesato, S. Yamazoe, D. Yokogawa, K. Yamaguchi and K. Suzuki, *Angew. Chem., Int. Ed.*, 2021, **60**, 16994–16998.
113 J. Zhuge, F. Rouhani, F. Bigdeli, X.-M. Gao, H. Kaviani, H.-J. Li, W. Wang, M.-L. Hu, K.-G. Liu and A. Morsali, *Dalton Trans.*, 2021, **50**, 2606–2615.
114 Q.-Y. Wang, J. Wang, S. Wang, Z.-Y. Wang, M. Cao, C.-L. He, J.-Q. Yang, S.-Q. Zang and T. C. W. Mak, *J. Am. Chem. Soc.*, 2020, **142**, 12010–12014.
115 C. Wang, Y.-J. Wang, C.-L. He, Q.-Y. Wang and S.-Q. Zang, *JACS Au*, 2021, **1**, 2202–2207.
116 H. Li, W. Duan, X. Cui, S. Liu, Y. Bai, Y.-X. Wang, S. Feng, Y. Wang, M. Qu and X.-M. Zhang, *ACS Appl. Nano Mater.*, 2022, **5**, 14251–14255.
117 J.-Y. Wang, Y.-K. Li, X. Jing, P. Luo, X.-Y. Dong and S.-Q. Zang, *ACS Mater. Lett.*, 2022, **4**, 960–966.
118 Z.-J. Guan, R.-L. He, S.-F. Yuan, J.-J. Li, F. Hu, C.-Y. Liu and Q.-M. Wang, *Angew. Chem., Int. Ed.*, 2022, **61**, e202116965.
119 J. Yuan, X. Huang, W. Zhang, M. Zhou, G. Li, F. Tian and R. Chen, *Inorg. Chem.*, 2023, **62**, 17668–17677.
120 K. Yonesato, D. Yanai, S. Yamazoe, D. Yokogawa, T. Kikuchi, K. Yamaguchi and K. Suzuki, *Nat. Chem.*, 2023, **15**, 940–947.
121 K. O. Sulaiman, A. Bueckert, A. Abdellah, S. K. Veeranmaril, D. C. Higgins and R. W. J. Scott, *J. Phys. Chem. C*, 2022, **126**, 16117–16126.
122 K. O. Sulaiman, V. Sudheeshkumar and R. W. J. Scott, *RSC Adv.*, 2019, **9**, 28019–28027.
123 L. Li, Y. Lv, H. Sheng, Y. Du, H. Li, Y. Yun, Z. Zhang, H. Yu and M. Zhu, *Nat. Commun.*, 2023, **14**, 6989.
124 T. U. B. Rao, B. Nataraju and T. Pradeep, *J. Am. Chem. Soc.*, 2010, **132**, 16304–16307.
125 T. Udayabhaskararao, M. S. Bootharaju and T. Pradeep, *Nanoscale*, 2013, **5**, 9404–9411.